Geophysical Journal International

*Geophys. J. Int.* (2012) **190,** 522–540 doi: 10.1111/j.1365-246X.2012.05495.x

# Finite-frequency structural sensitivities of short-period compressional body waves

Nobuaki Fuji,[1,2] Sébastien Chevrot,[1,2] Li Zhao,[3] Robert J. Geller[4] and Kenji Kawai[5]

[1] *Université de Toulouse, UPS-OMP, IRAP, Toulouse, France. E-mail: Nobuaki.Fuji@irap.omp.eu*
[2] *IRAP; CNRS,* UMR5277, 14, *Avenue Edouard Belin,* F-31400 *Toulouse, France*
[3] *Institute of Earth Sciences, Academia Sinica, Taipei, Taiwan*
[4] *Department of Earth and Planetary Science, Graduate School of Science, the University of Tokyo, Tokyo, Japan*
[5] *Department of Earth and Planetary Sciences, Tokyo Institute of Technology, Tokyo, Japan*

Accepted 2012 April 4. Received 2012 March 29; in original form 2011 October 12

## SUMMARY

We present an extension of the method recently introduced by Zhao & Chevrot for calculating Fréchet kernels from a precomputed database of strain Green's tensors by normal mode summation. The extension involves two aspects: (1) we compute the strain Green's tensors using the Direct Solution Method, which allows us to go up to frequencies as high as 1 Hz; and (2) we develop a spatial interpolation scheme so that the Green's tensors can be computed with a relatively coarse grid, thus improving the efficiency in the computation of the sensitivity kernels. The only requirement is that the Green's tensors be computed with a fine enough spatial sampling rate to avoid spatial aliasing. The Green's tensors can then be interpolated to any location inside the Earth, avoiding the need to store and retrieve strain Green's tensors for a fine sampling grid. The interpolation scheme not only significantly reduces the CPU time required to calculate the Green's tensor database and the disk space to store it, but also enhances the efficiency in computing the kernels by reducing the number of I/O operations needed to retrieve the Green's tensors. Our new implementation allows us to calculate sensitivity kernels for high-frequency teleseismic body waves with very modest computational resources such as a laptop. We illustrate the potential of our approach for seismic tomography by computing traveltime and amplitude sensitivity kernels for high frequency *P, PKP* and $P_{\mathrm{diff}}$ phases. A comparison of our *PKP* kernels with those computed by asymptotic ray theory clearly shows the limits of the latter. With ray theory, it is not possible to model waves diffracted by internal discontinuities such as the core–mantle boundary, and it is also difficult to compute amplitudes for paths close to the B-caustic of the *PKP* phase. We also compute waveform partial derivatives for different parts of the seismic wavefield, a key ingredient for high resolution imaging by waveform inversion. Our computations of partial derivatives in the time window where *PcP* precursors are commonly observed show that the distribution of sensitivity is complex and counter-intuitive, with a large contribution from the mid-mantle region. This clearly emphasizes the need to use accurate and complete partial derivatives in waveform inversion.

**Key words:** Body waves; Seismic tomography; Theoretical seismology; Wave propagation.

GJI Seismology

## 1 INTRODUCTION

In seismic tomography, the resolution potential of a given data set depends critically on both spatial coverage and frequency content of seismic waves amongst other things. High resolution images of the mantle have been obtained in the past by inverting the global data set of the International Seismological Centre (e.g. van der Hilst *et al.* 1997; Bijwaard *et al.* 1998), which contains millions of compressional wave arrival times picked for the most part on short period records. In spite of the tremendous size of this data set, the resolution was still limited by uneven ray coverage, as a large part of the Earth's mantle is poorly sampled, and by the level of noise in traveltime data. With the ever-increasing number of temporary and permanent broadband stations worldwide, spatial coverage and consequently resolution is expected to improve dramatically in many parts of the mantle. To further improve our tomographic images of the Earth's interior, it is now necessary to build high quality global data sets of traveltime and amplitude measurements by exploiting the waveforms of a large number of seismic phases. Such an effort is currently underway, and the results will be reported soon in a forthcoming publication. To fully exploit this new data set, it is also necessary to develop efficient numerical methods to compute the

exact sensitivity to 3-D structure of such traveltime and amplitude measurements. This is particularly challenging for the case of *P* or *PKP* waves, because the computations must be performed for periods as short as 1 s, around which these waves are best observed on seismic records.

Finite-frequency kernels can in principle be computed exactly in 3-D Earth models (e.g. Tromp *et al.* 2005; Zhao *et al.* 2005; Sieminski *et al.* 2007; Fichtner *et al.* 2008; Liu & Tromp 2008). However, these approaches require extremely large computational resources even at periods much longer than our target of 1 s, which prevents their application to massive *P*-wave traveltime data sets. Dahlen *et al.* (2000) proposed an algorithm based upon far-field asymptotic solutions of the wave equation (ray theory) to make calculations of traveltime kernels for high frequency body waves tractable. A few tomographic studies subsequently used this approach to incorporate 3-D traveltime kernels into global tomography studies (e.g. Montelli *et al.* 2004). While the asymptotic approach (Dahlen *et al.* 2000) accounts for finite-frequency effects on traveltimes and amplitudes, it still suffers from important shortcomings. First, ray theory can not be used to describe diffracted waves such as $P_{\rm diff}$ or $S_{\rm diff}$. This considerably limits our ability to image structures in the lowermost mantle, since waves diffracted by the core have the strongest sensitivity to structural heterogeneity at the base of the mantle. Secondly, neglecting the contribution of the near field can potentially bias traveltime sensitivity kernels in the vicinity of sources and stations, as shown by Favier *et al.* (2004). Thirdly, asymptotic approximations do not fully describe the complexity of wavefields and it is often cumbersome to account for all the seismic phases that can contribute to the observed signal in the time window of interest. Finally, the computation of wave amplitudes with ray theory is difficult and requires interpolation of the spherical velocity model (Calvet & Chevrot 2005). This problem is important because inaccurate seismic amplitudes translate into errors in traveltime sensitivity kernels, and thus into biases in tomographic models. From this short overview, it is clear that there is a need to develop efficient numerical methods for computing exact sensitivity kernels.

A solution to this problem was proposed by Zhao & Chevrot (2011a) who showed that partial derivatives can be expressed as convolutions of the components of two types of strain Green's tensors (SGTs), emanating from the source and back-propagated from the receiver. These SGTs can be precalculated with any simulation method and stored in a database, so that they can be retrieved to compute partial derivatives very efficiently. Zhao & Chevrot (2011b) computed the SGTs by normal-mode summation and showed examples of kernel computations for various seismological observables on both body and surface waves. Because it is difficult to compute spheroidal modes at periods shorter than 8 s, they could only compute body wave kernels at relatively long periods.

Here, we will use the Direct Solution Method (DSM) to compute the SGT database, with the objective of being able to compute sensitivity kernels at periods as short as 1 s. The DSM is a Galerkin method that solves the weak form of the elastic equation of motion in the frequency domain (e.g. Geller & Ohminato 1994; Geller & Takeuchi 1995). By carefully tuning the vertical grid spacing, maximum angular order, and cut-off depth, the calculations can be made very efficient while keeping high accuracy, even at frequencies as high as 2 Hz (Kawai *et al.* 2006). We first describe this method and derive the expressions of SGTs from the numerical solutions for displacement. We then explain an important improvement of our initial implementation that consists of interpolating SGTs, thereby avoiding the need to compute and store the SGT database in a grid with fine distance and depth sampling rates. This saves storage space and limits the volume of data that needs to be read for computing the sensitivity kernels. Another improvement comes from an adaptive algorithm that determines the domain where the values of the partial derivatives are significant, thereby avoiding the unnecessary computation of the kernels outside the first Fresnel zones. We illustrate our approach by computing Fréchet kernels for the traveltimes and amplitudes of high frequency *P*, *PKP* and $P_{\rm diff}$ phases. Finally, we compute waveform partial derivatives for different parts of the seismic wavefield and demonstrate their potential for high resolution imaging of the deep Earth by migration and waveform inversion.

## 2 PARTIAL DERIVATIVES EXPRESSED IN TERMS OF STRAIN GREEN'S TENSORS

### 2.1 Fréchet kernels expressed in terms of strain Green's tensors

The perturbation of the displacement from a source $\mathbf{r}_S$ to a receiver $\mathbf{r}_R$ due to structural perturbations at $\mathbf{r}_Q$ can be obtained by the convolution of the forward-propagating field at $\mathbf{r}_Q$ from $\mathbf{r}_S$ and the adjoint (time-reversed back-propagated) field from $\mathbf{r}_R$ (e.g. Geller & Hara 1993). In the frequency domain, this can be expressed as

$$\delta u_n(\mathbf{r}_Q,\omega;\mathbf{r}_R;\mathbf{r}_S) = \omega^2 u_i(\mathbf{r}_Q,\omega;\mathbf{r}_S)\delta\rho(\mathbf{r}_Q)g^*_{in}(\mathbf{r}_Q,\omega;\mathbf{r}_R) - u_{i,j}(\mathbf{r}_Q,\omega;\mathbf{r}_S)\delta\Lambda_{ijkl}(\mathbf{r}_Q,\omega)g^*_{kn,l}(\mathbf{r}_Q,\omega;\mathbf{r}_R), \quad (1)$$

where $u_i(\mathbf{r}_Q,\omega;\mathbf{r}_S)$ is the $i$-component of the forward propagated displacement at $\mathbf{r}_Q$ excited by a source $\mathbf{r}_S$ (either a double couple or a force), and $g_{in}(\mathbf{r}_Q,\omega;\mathbf{r}_R)$ is the Green's tensor, that is, the $i$-component displacement at $\mathbf{r}_Q$ excited by a unit impulsive force applied in the $n$-direction at $\mathbf{r}_R$. Note that an asterisk superscript denotes complex conjugation. $\delta\rho(\mathbf{r}_Q)$ and $\delta\Lambda_{ijkl}(\mathbf{r}_Q,\omega)$ are the perturbations to the density and elastic tensor, respectively. The geometry of the locations $\mathbf{r}_S$, $\mathbf{r}_R$ and $\mathbf{r}_Q$ in the Earth and their projections onto the surface of the sphere are shown in Fig. 1. Einstein's summation rule is assumed throughout this paper. A comma in the

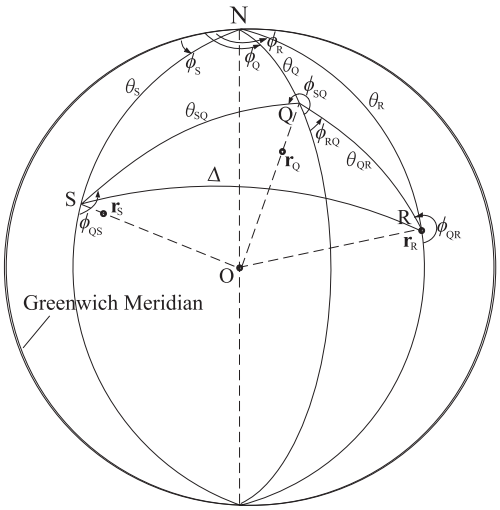


**Figure 1.** Geometry of the source at $\mathbf{r}_S$, receiver at $\mathbf{r}_R$ and an arbitrary location $\mathbf{r}_Q$ at which the Fréchet kernel is calculated (from Zhao & Chevrot 2011a). s, R and Q are the surface projections of $\mathbf{r}_S$, $\mathbf{r}_R$ and $\mathbf{r}_Q$, respectively. Here $\mathbf{r}_R$ and R coincide, since the receiver is assumed to be on the surface.

subscript indicates spatial differentiation. For example,

$$u_{i,j} = \frac{\partial u_i}{\partial x_j}$$

is the local Cartesian derivative. Using the symmetry property of the elasticity tensor

$$\Lambda_{ijkl} = \Lambda_{jikl} = \Lambda_{ijlk} = \Lambda_{klij}, \tag{2}$$

and focusing only on the perturbation of the elastic tensor, we can further simplify eq. (1) as

$$\delta u_n(\mathbf{r}_Q, \omega) = -\epsilon_{ij}(\mathbf{r}_Q, \omega; \mathbf{r}_S)\delta\Lambda_{ijkl}(\mathbf{r}_Q, \omega)h_{nkl}(\mathbf{r}_R, \omega; \mathbf{r}_Q), \tag{3}$$

where $\epsilon_{ij}(\mathbf{r}_Q, \omega; \mathbf{r}_S)$ denotes the $(i,j)$-component of the strain of the forward field $u_i(\mathbf{r}_Q, \omega; \mathbf{r}_S)$

$$\epsilon_{ij} = \tfrac{1}{2}(u_{i,j} + u_{j,i}), \tag{4}$$

and $h_{nkl}(\mathbf{r}_R, \omega; \mathbf{r}_Q)$ is the $(k, l)$-component of the strain associated with the Green's tensor $g_{kn}(\mathbf{r}_Q, \omega; \mathbf{r}_R)$, that is, the single-side SGT defined in Zhao & Chevrot (2011a)

$$h_{nkl}(\mathbf{r}_R, \omega; \mathbf{r}_Q) = \tfrac{1}{2}\left[g^*_{kn,l}(\mathbf{r}_Q, \omega; \mathbf{r}_R) + g^*_{ln,k}(\mathbf{r}_Q, \omega; \mathbf{r}_R)\right]. \tag{5}$$

The forward strain field $\epsilon_{ij}$ produced by a moment tensor $M_{pq}$ at $\mathbf{r}_S$ can be expressed as

$$\epsilon_{ij}(\mathbf{r}_Q, \omega; \mathbf{r}_S) = M_{pq}H_{ijpq}(\mathbf{r}_Q, \omega; \mathbf{r}_S), \tag{6}$$

where $H_{ijpq}$ is the two-side SGT defined in Zhao & Chevrot (2011a).

The DSM accounts for the effect of anelasticity in an exact manner (Fuji *et al.* 2010). Therefore eq. (3) can be used to model the displacement perturbation due to a general complex perturbation to the elastic tensor, including the effects of perturbations in physical dispersion and attenuation. In this study, however, for simplicity, we only consider elastic perturbations relative to an anelastic reference model, that is, $\delta\Lambda_{ijkl}$ is real and frequency independent.

For the perfectly elastic case, substituting eq. (6) into eq. (3) and transforming it to the time domain, we obtain the same expression of Zhao & Chevrot (2011a,b) for the waveform perturbation density

$$\delta u_n(\mathbf{r}_Q, t) = -h_{nkl}(\mathbf{r}_R, t; \mathbf{r}_Q) * H_{ijpq}(\mathbf{r}_Q, t; \mathbf{r}_S)M_{pq}\delta\Lambda_{ijkl}(\mathbf{r}_Q). \tag{7}$$

In this expression, $\mathbf{h}(\mathbf{r}_R, t; \mathbf{r}_Q)$ is the third-order Single-side Strain Green's Tensor (SSGT) whose elements $h_{ijk}$ represent the $(j, k)$-component of the strain field at $\mathbf{r}_Q$ due to an impulsive point force acting at $\mathbf{r}_R$ along direction $i$-direction. Similarly, $\mathbf{H}(\mathbf{r}_Q, t; \mathbf{r}_S)$ is the fourth-order Two-side Strain Green's Tensor (TSGT) whose elements $H_{ijkl}$ represent the $(i, j)$-component of the strain field at $\mathbf{r}_Q$ due to an elementary double couple source $M_{kl}$ applied at $\mathbf{r}_S$. Note that the symbol $*$ denotes convolution in time. The waveform perturbation density in eq. (7) is the fundamental quantity to consider in the derivation of partial derivatives. For example, the partial derivative of a waveform at location $\mathbf{r}_Q$ and time $t$ with respect to a perturbation $\delta\Lambda_{ijkl}$ of the elasticity tensor is simply

$$K^{u_n}_{\Lambda_{ijkl}}(\mathbf{r}_Q, t) = \left(\frac{\delta u_n}{\delta\Lambda_{ijkl}}\right)(\mathbf{r}_Q, t) = -h_{nji}(\mathbf{r}_R, t; \mathbf{r}_Q) * H_{klpq}(\mathbf{r}_Q, t; \mathbf{r}_S)M_{pq}. \tag{8}$$

Using the partial derivatives in eq. (8), we can derive the expressions for the Fréchet kernels of any seismic observables derived through linear operations of waveform. For example, the expression of the sensitivity kernel for the traveltime of a seismic phase obtained by cross-correlation of observed and synthetic seismograms in the time interval $[t_1, t_2]$ can be written as (Dahlen *et al.* 2000)

$$K^{T_n}_{\Lambda_{ijkl}}(\mathbf{r}_Q) = \int_{t_1}^{t_2} J^{T_n}(\mathbf{r}_R, t; \mathbf{r}_S)K^{u_n}_{\Lambda_{ijkl}}(\mathbf{r}_Q, t)\,\mathrm{d}t. \tag{9}$$

We can taper the time window so that the amplitude of the seismic phase being measured is zero at both ends of the time window, this leads to

$$J^{T_n}(\mathbf{r}_R, t; \mathbf{r}_S) = -\frac{\partial_t u_n(\mathbf{r}_R, t; \mathbf{r}_S)}{\int_{t_1}^{t_2}[\partial_t u_n(\mathbf{r}_R, t; \mathbf{r}_S)]^2\,\mathrm{d}t}, \tag{10}$$

while the amplitude kernel takes the form:

$$K^{\ln A_n}_{\Lambda_{ijkl}}(\mathbf{r}_Q) = \int_{t_1}^{t_2} J^{\ln A_n}(\mathbf{r}_R, t; \mathbf{r}_S)K^{u_n}_{\Lambda_{ijkl}}(\mathbf{r}_Q, t)\,\mathrm{d}t \tag{11}$$

with

$$J^{\ln A_n}(\mathbf{r}_R, t; \mathbf{r}_S) = \frac{u_n(\mathbf{r}_R, t; \mathbf{r}_S)}{\int_{t_1}^{t_2}[u_n(\mathbf{r}_R, t; \mathbf{r}_S)]^2\,\mathrm{d}t}. \tag{12}$$

Therefore, to compute the value of a Fréchet kernel at an arbitrary location, we only need to know the elements of the third-order SSGT **h** and fourth-order TSGT **H**.

### 2.2 *P*-wave kernels

From now on, we will focus on the computation of kernels for high-frequency *P* waves. These waves are mostly sensitive to $\alpha$, the compressional wave velocity. An isotropic elasticity tensor is given by

$$\Lambda_{ijkl} = \lambda\delta_{ij}\delta_{kl} + \mu(\delta_{ik}\delta_{jl} + \delta_{il}\delta_{jk}), \tag{13}$$

where $\lambda$ and $\mu$ are the Lamé parameters, and $\delta_{ij}$ denotes the Kronecker delta. Substituting eq. (13) into eq. (7) and using the relation between the perturbations of *P*-wave speed and elastic moduli

$$2\rho\alpha\delta\alpha = \delta\lambda + 2\delta\mu, \tag{14}$$

we obtain the partial derivative of the $n$-component waveform for $\alpha$

$$K^{u_n}_{\alpha}(\mathbf{r}_Q, t) = \left(\frac{\delta u_n}{\delta\alpha}\right)(\mathbf{r}_Q, t) \tag{15}$$

$$= -2\rho\alpha(h_{nrr} + h_{n\theta\theta} + h_{n\phi\phi}) * (H_{rrpq} + H_{\theta\theta pq} + H_{\phi\phi pq})M_{pq}, \tag{16}$$

where for brevity the spatial and temporal dependence of the SGTs is omitted. From this expression, it can be seen that to compute *P*-wave kernels we only need the trace of the second-order strain tensor part of SSGT and TSGT at location $\mathbf{r}_Q$. In addition, since *P* waves are generally observed on vertical components, it is sufficient to compute the components of the SSGT **h** corresponding to $n = r$.

### 2.3 Construction of a strain Green's tensor database

The numerical efficiency of our approach relies on the fact that we can evaluate expressions such as (16) by using a pre-calculated database of SGTs. For example, as shown in Fig. 1, if we can calculate in advance the TSGT **H** for all possible locations of $\mathbf{r}_S$ and $\mathbf{r}_Q$ and establish a database, then in the evaluation of any Fréchet kernels we can simply retrieve the TSGTs from the database, thus achieving a better efficiency. In general, each element of the TSGT **H** is a function of six variables: the 3-D coordinates of $\mathbf{r}_S$ and

$\mathbf{r}_Q$. As a result, the amount of computation and storage for the TSGT database are huge and can only be applied on small-scale studies (e.g. Zhao *et al.* 2006; Chen *et al.* 2007). However, for a spherically symmetric Earth model, the TSGT $\mathbf{H}$ only varies with four parameters: $r_S$ and $r_Q$, the arc distance $\Delta_{SQ}$, and the angle $\phi_{QS}$. Furthermore, the spherical symmetry leads to the decoupling of the dependence on $\phi_{QS}$ from the other three variables. As a result, we can establish a TSGT database with all its elements sampled for a set of ($r_S$, $r_Q$, $\Delta_{QS}$) values. The dependence on $\phi_{QS}$, all in the form of its sines and cosines, can easily be taken into account during the kernel calculations.

In actual implementation, the TSGT elements in the database are calculated in a spherical polar system in which $\mathbf{r}_S$ is on the north pole and the arc $SQ$ coincides with zero longitude. Then, when we use eq. (16) to compute the kernel, we need to first rotate the coordinate system at $\mathbf{r}_S$ by the angle $\phi_{QS}$. Note that this rotation transforms the last two indices of the fourth-order TSGT, that is,

$$H_{ijpq} = R_{pp'} R_{qq'} \tilde{H}_{ijp'q'}, \tag{17}$$

where $\mathbf{R}$ is the rotation matrix corresponding to a rotation of angle $\phi_{QS}$ around the vertical axis, and $\tilde{\mathbf{H}}$ is the TSGT calculated and stored in the database. We thus obtain

$$H_{ijrr} = \tilde{H}_{ijrr} \tag{18}$$

$$H_{ijr\theta} = \tilde{H}_{ijr\theta} \cos\phi_{QS} \tag{19}$$

$$H_{ijr\phi} = \tilde{H}_{ijr\theta} \sin\phi_{QS} \tag{20}$$

$$H_{ij\theta\theta} = \tfrac{1}{2}(\tilde{H}_{ij\theta\theta} + \tilde{H}_{ij\phi\phi}) + \tfrac{1}{2}(\tilde{H}_{ij\theta\theta} - \tilde{H}_{ij\phi\phi}) \cos 2\phi_{QS} \tag{21}$$

$$H_{ij\theta\phi} = \tfrac{1}{2}(\tilde{H}_{ij\theta\theta} - \tilde{H}_{ij\phi\phi}) \sin 2\phi_{QS} \tag{22}$$

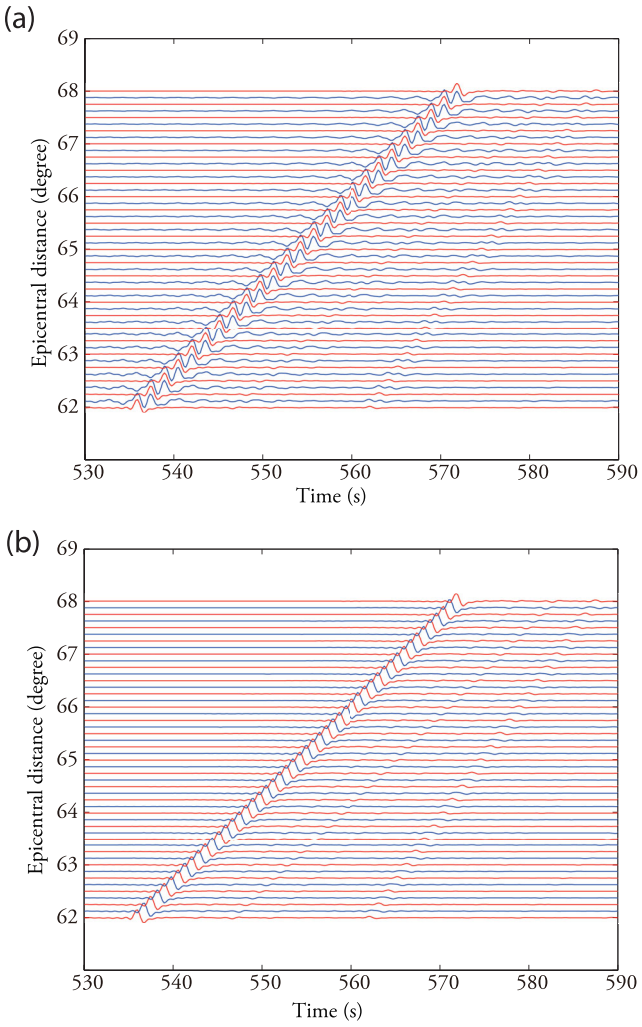


**Figure 2.** Interpolation of *P* wave Green's function. The 'exact' Single-Side Green's Tensors (red lines) are calculated with DSM at 20 km depth. The blue lines show the interpolated Single-Side Green's Tensors without (top panel) and with (bottom panel) normal move-out corrections for a slowness of 6.51 s deg$^{-1}$ which corresponds to a *P* wave observed at an epicentral distance of 65°. All the traces are bandpass filtered between 0.1 and 1.0 Hz. Note the strong spatial aliasing on the interpolated traces when the normal move-out corrections are omitted.

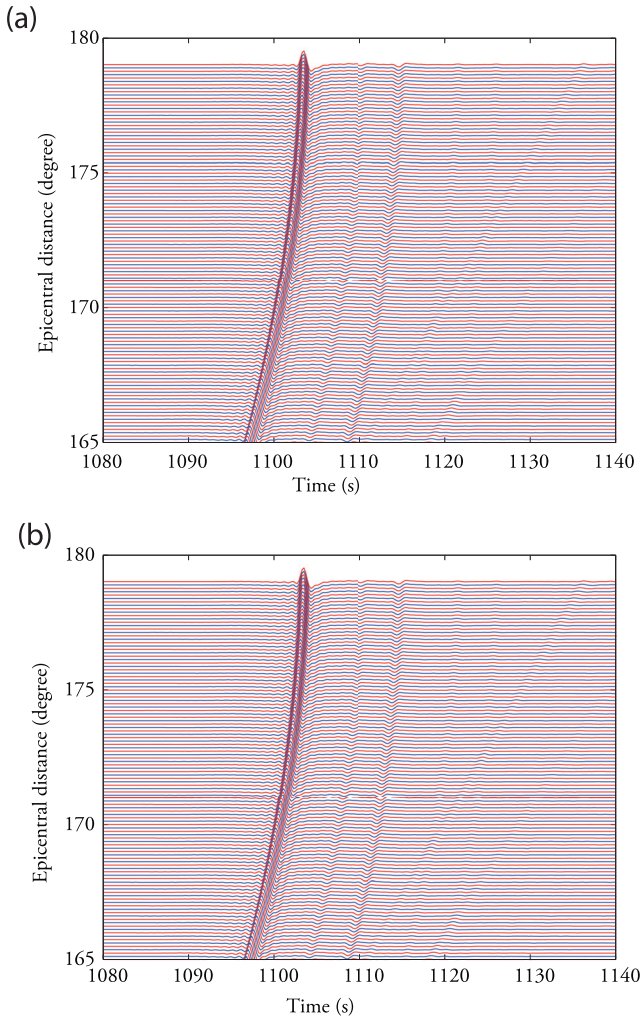


**Figure 3.** Interpolation of *PKP*df wave Green's functions. The 'exact' Single-Side Green's Tensors (red lines) are calculated with DSM at 1000 km depth. The blue lines show the interpolated Single-Side Green's Tensors without (top panel) and with (bottom panel) normal move-out corrections for a slowness of 0.24 s deg$^{-1}$ which corresponds to a *PKP*df wave observed at an epicentral distance of 176°. All the traces are bandpass filtered between 0.1 and 1.0 Hz. Note the absence of spatial aliasing on the interpolated traces when the normal move-out corrections are omitted.

$$H_{ij\phi\phi} = \tfrac{1}{2}(\tilde{H}_{ij\theta\theta} + \tilde{H}_{ij\phi\phi}) - \tfrac{1}{2}(\tilde{H}_{ij\theta\theta} - \tilde{H}_{ij\phi\phi})\cos 2\phi_{QS}. \quad (23)$$

In deriving these expressions, the contributions of $\tilde{H}_{ijr\phi}$ and $\tilde{H}_{ij\theta\phi}$ have been omitted, because they only contribute to the *SH* wavefield. Since the TSGT is a two-point tensor, a similar rotation of angle $\phi_{SQ}$ at $\mathbf{r}_Q$ is also needed to transform the first two indices of $\tilde{\mathbf{H}}$. Therefore, in general both $\phi_{QS}$ and $\phi_{SQ}$ are needed to transform the TSGT in the database $\tilde{\mathbf{H}}$ to the one used in eq. (16). However, for the vertical-component $P$ waves we consider in this study, terms involving $\phi_{SQ}$ cancel out.

The third-order SSGT $\mathbf{h}$ is also a two-point tensor and in practice its database involves its elements sampled on a set of ($r_Q$, $r_R = a$, $\Delta_{QR}$) values, where $a$ is simply the Earth's radius. Similar to the TSGT, coordinate rotations are required at $\mathbf{r}_Q$ and $\mathbf{r}_R$ to transform the SSGT in the database $\tilde{\mathbf{h}}$ to that in eq. (16). Again, for vertical-component $P$ waves all terms involving rotation angles cancel out, and we obtain the sensitivity of the vertical $P$ wave to $P$-wave speed

$$K_\alpha^{u_r} = -2\rho\alpha\tilde{h}(\Delta_{RQ}, r_Q) * \Big[\mathcal{H}_1 M_{rr} + \frac{\mathcal{H}_2 + \mathcal{H}_3}{2}(M_{\theta\theta} + M_{\phi\phi}) + \frac{\mathcal{H}_2 + \mathcal{H}_3}{2}(M_{\theta\theta} - M_{\phi\phi})\cos 2\phi_{QS} + \frac{\mathcal{H}_2 - \mathcal{H}_3}{2} M_{\theta\phi} \sin 2\phi_{QS} + \mathcal{H}_4 M_{r\theta} \cos\phi_{QS} + \mathcal{H}_4 M_{r\phi} \sin\phi_{QS}\Big], \quad (24)$$

where

$$\mathcal{H}_1 = \tilde{H}_{rrrr} + \tilde{H}_{\theta\theta rr} + \tilde{H}_{\phi\phi rr} \quad (25)$$

$$\mathcal{H}_2 = \tilde{H}_{rr\theta\theta} + \tilde{H}_{\theta\theta\theta\theta} + \tilde{H}_{\phi\phi\theta\theta} \quad (26)$$

$$\mathcal{H}_3 = \tilde{H}_{rr\phi\phi} + \tilde{H}_{\theta\theta\phi\phi} + \tilde{H}_{\phi\phi\phi\phi} \quad (27)$$

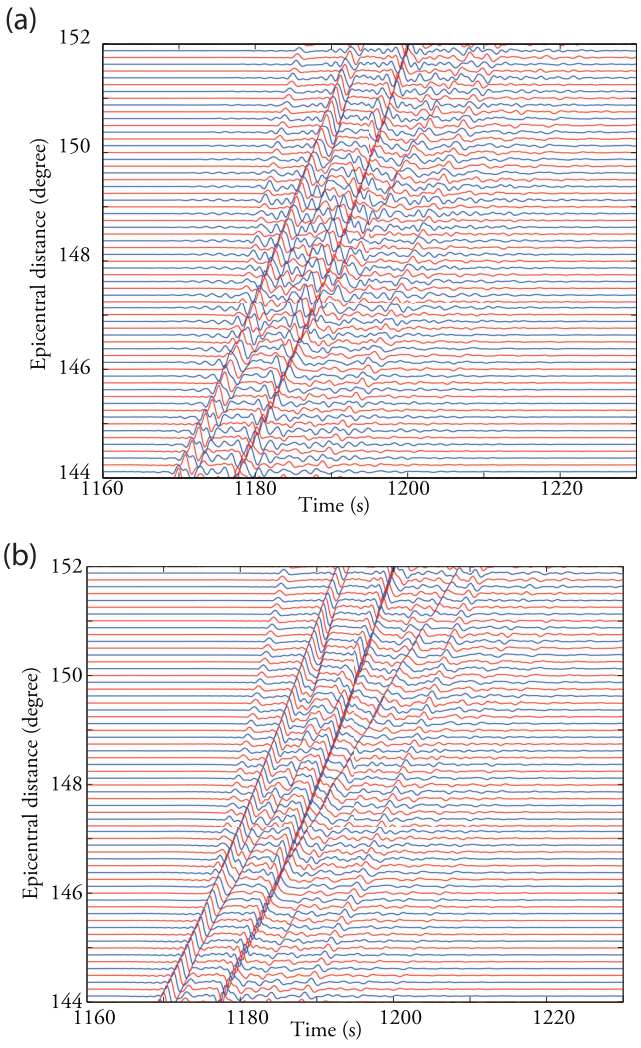


**Figure 4.** Interpolation of Green's function around the *PKP* triplication. The 'exact' Single-Side Green's Tensors (red lines) are calculated with DSM at 20 km depth. The blue lines show the interpolated Single-Side Green's Tensors without (top panel) and with (bottom panel) normal move-out corrections for a slowness of 2.56 s deg$^{-1}$ which corresponds to a *PKP*bc wave observed at an epicentral distance of 150°. All the traces are bandpass filtered between 0.1 and 1.0 Hz. Note the strong spatial aliasing on the interpolated traces when the normal move-out corrections are omitted.

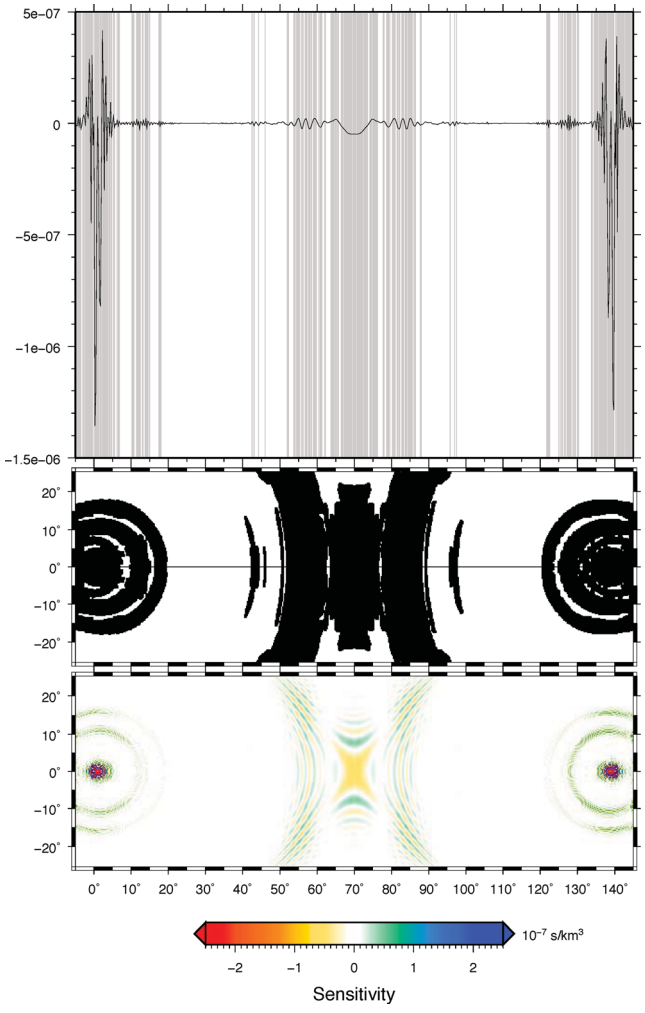


**Figure 5.** Illustration of the algorithm to compute the sensitivity kernels. In this example, we compute the traveltime sensitivity kernel at 200 km depth for a *PP* wave bandpass filtered between 0.01 and 0.1 Hz produced by an explosive source at 20 km depth at an epicentral distance of 140°. At each depth, we first detect the position of the significant values of the kernel along the great-circle path (grey regions on the top plot). These domains are then explored and extended along latitudinal lines when moving away from the great-circle path. The kernels are computed only inside these significant domains, marked in black in the middle plot. The bottom plot shows the *PP* sensitivity kernel at 200 km depth computed with this algorithm.

$$\mathcal{H}_4 = \tilde{H}_{rr r\theta} + \tilde{H}_{\theta\theta r\theta} + \tilde{H}_{\phi\phi r\theta}. \quad (28)$$

Here, $\mathcal{H}_1$ is the trace of strain at distance $\Delta_{QS}$ and radius $r_Q$ produced by an elementary double couple $M_{rr}$ at radius $r_S$. Similarly, the other components $\mathcal{H}_2$, $\mathcal{H}_3$ and $\mathcal{H}_4$, are for elementary double couple sources $M_{\theta\theta}$, $M_{\phi\phi}$ and $M_{r\theta}$, respectively. We point out that eq. (24) can be derived from a simplification of the general relations given in the appendices of Zhao & Chevrot (2011a).

In general, as demonstrated by Zhao & Chevrot (2011a), the computation of partial derivatives requires 10 components for $\tilde{h}$ and 20 components for $\tilde{H}$. However, for the particular case of $P$ waves, our derivation shows that only one component is actually required for $\tilde{h}$ and four components for $\tilde{H}$ (that we name $\mathcal{H}$). Therefore, it is possible to design an optimal database of SGTs for the computation of $P$ wave partial derivatives. Another advantage of defining specific databases for each type of seismic phase is that we can fine tune the time (or frequency) and spatial samplings in the computation of the SGTs. We explain in the next section how these strain tensors can be computed with the DSM.

## 3 COMPUTATION OF STRAIN GREEN'S TENSORS WITH THE DIRECT SOLUTION METHOD

### 3.1 The direct solution method

We express the displacement as a linear combination of $N$ vector trial functions $\phi_i^{(n)}$

$$u_i(\mathbf{r}) = \sum_{n=1}^{N} c_n \phi_i^{(n)}(\mathbf{r}). \quad (29)$$

We use linear spline functions $X_k(r)$ for the vertical dependence of the displacement

$$X_k(r) = \begin{cases} (r - r_{k-1})/(r_k - r_{k-1}) & : \quad r_{k-1} < r \leq r_k \\ (r_{k+1} - r)/(r_{k+1} - r_k) & : \quad r_k \leq r < r_{k+1} \\ 0 & : \quad \text{otherwise} \end{cases} \quad (30)$$

and complex vector spherical harmonics $\mathbf{S}_{lm}^1$, $\mathbf{S}_{lm}^2$ and $\mathbf{T}_{lm}$ to describe the lateral dependence of the displacement

$$\mathbf{S}_{lm}^1(\theta,\phi) = (Y_{lm}(\theta,\phi), 0, 0)$$

$$\mathbf{S}_{lm}^2(\theta,\phi) = \left(0, \frac{1}{\mathcal{L}}\frac{\partial Y_{lm}(\theta,\phi)}{\partial\theta}, \frac{1}{\mathcal{L}\sin\theta}\frac{\partial Y_{lm}(\theta,\phi)}{\partial\phi}\right)$$

$$\mathbf{T}_{lm}(\theta,\phi) = \left(0, \frac{1}{\mathcal{L}\sin\theta}\frac{\partial Y_{lm}(\theta,\phi)}{\partial\phi}, -\frac{1}{\mathcal{L}}\frac{\partial Y_{lm}(\theta,\phi)}{\partial\theta}\right),$$

where $Y_{lm}(\theta,\phi)$ are fully normalized spherical harmonics and $\mathcal{L} = \sqrt{l(l+1)}$ (Takeuchi & Saito 1972; Takeuchi *et al.* 1996). In this vector spherical harmonics basis, the displacement vector is given by

$$\mathbf{u}(r,\theta,\phi) = \sum_{lm} U_{lm}(r)\mathbf{S}_{lm}^1 + V_{lm}(r)\mathbf{S}_{lm}^2 + W_{lm}(r)\mathbf{T}_{lm}, \quad (31)$$

where the radial functions are related to the radial trial functions through

$$U_{lm}(r) = \sum_k c_{lmk}^1 X_k(r) \quad (32)$$

$$V_{lm}(r) = \sum_k c_{lmk}^2 X_k(r) \quad (33)$$

$$W_{lm}(r) = \sum_k c_{lmk}^3 X_k(r). \quad (34)$$

The weak form of the equation of motion can be written as

$$\omega^2 \int_V \phi_i^{*(m)} \rho u_i \, \mathrm{d}V - \int_V \phi_{i,j}^{*(m)} \Lambda_{ijkl} u_{k,l} \, \mathrm{d}V + \int_S \phi_i^{*(m)} S_{ij} u_j \, \mathrm{d}S = -\int_V \phi_i^{*(m)} f_i \, \mathrm{d}V \quad (35)$$

with $\rho$ and $\Lambda$, respectively the density and the fourth-order elasticity tensor, and $\mathbf{f}$ the excitation of the earthquake. Note that DSM can handle attenuation effects with no additional cost. In this expression, superscript $*$ denotes the complex conjugate. By substituting eq. (29) into eq. (35), we obtain the Galerkin weak form of the equation of motion

$$(\omega^2\mathbf{T} - \mathbf{H} + \omega\mathbf{R})\mathbf{c} = -\mathbf{g}, \quad (36)$$

where $\mathbf{T}$ is the mass matrix, $\mathbf{H}$ is the stiffness matrix, $\mathbf{g}$ is the force vector and $\mathbf{R}$ is an operator which enforces continuity conditions at fluid-solid boundaries. The elements of the matrices in eq. (36) are given by

$$T_{mn} = \int_V \phi_i^{*(m)} \rho \phi_i^{(n)} \, \mathrm{d}V \quad (37)$$

$$H_{mn} = \int_V \phi_{i,j}^{*(m)} \Lambda_{ijkl} \phi_{k,l}^{(n)} \, \mathrm{d}V \quad (38)$$

$$R_{mn} = \int_S \phi_i^{*(m)} S_{ij} \phi_j^{(n)} \, \mathrm{d}S \quad (39)$$

$$g_m = \int_V \phi_i^{*(m)} f_i \, \mathrm{d}V. \quad (40)$$

This equation is directly solved to find the expansion coefficients of displacement contained in vector $\mathbf{c}$.

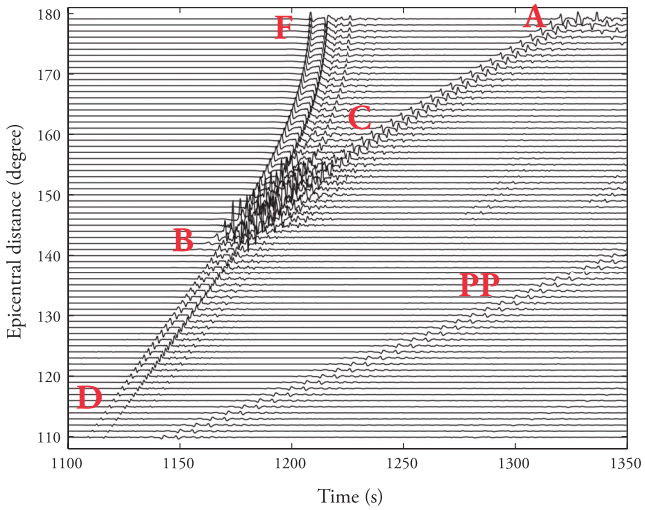


**Figure 6.** *PKP* waveforms (vertical component) with an explosive source at 20 km depth around their triplication. For epicentral distances between 142 and 155°, three *PKP* branches are recorded: *PKP*df, *PKP*bc, and *PKP*ab. To show the real amplitudes, the traces are not normalized. Note the strong amplification of *PKP*ab and *PKP*bc phases in this distance range resulting from the B-caustic.

### 3.2 Computation of strain from the displacement solution

From the solution for displacement obtained using the DSM in eq. (29), we can derive the expressions for the various components of the SGTs. Since we only need the trace of the strain tensor, we need to compute

$$\frac{\partial u_r}{\partial r} = \frac{\mathrm{d}U_{lm}(r)}{\mathrm{d}r} Y_{lm}(\theta, \phi) \tag{41}$$

$$\frac{\partial u_\theta}{\partial \theta} = \frac{1}{\mathcal{L}} \frac{\partial^2 Y_{lm}(\theta, \phi)}{\partial \theta^2} V_{lm}(r) \tag{42}$$

$$\frac{\partial u_\phi}{\partial \phi} = \frac{1}{\mathcal{L} \sin\theta} \frac{\partial^2 Y_{lm}(\theta, \phi)}{\partial \phi^2} V_{lm}(r). \tag{43}$$

Note that in these expressions we only kept the contributions of $\mathbf{S}^1_{lm}$ and $\mathbf{S}^2_{lm}$ which correspond to the *P-SV* wavefield and dropped the terms in $\mathbf{T}_{lm}$ which correspond to the *SH* wavefield. The derivatives of displacement with respect to $\phi$ and $\theta$ are obtained analytically, using the following identities

$$\frac{\partial P_{lm}(\theta)}{\partial \theta} = m \cot\theta P_{lm}(\theta) - P_{lm+1}(\theta) \tag{44}$$

$$\frac{\partial^2 Y_{lm}(\theta, \phi)}{\partial \phi^2} = -m^2 Y_{lm}(\theta, \phi) \tag{45}$$

$$\frac{\partial^2 Y_{lm}(\theta, \phi)}{\partial \theta^2} = -\left(\cot\theta \frac{\partial}{\partial \theta} - \frac{m^2}{\sin^2\theta} + \mathcal{L}^2\right) Y_{lm}(\theta, \phi). \tag{46}$$

To derive derivatives of displacement with respect to the vertical direction, we use a three-point interpolation algorithm (Suetsugu *et al.* 2005; Kawai & Geller 2010a). Since vertical strain is discontinuous at a discontinuity, we do not mix the displacements in

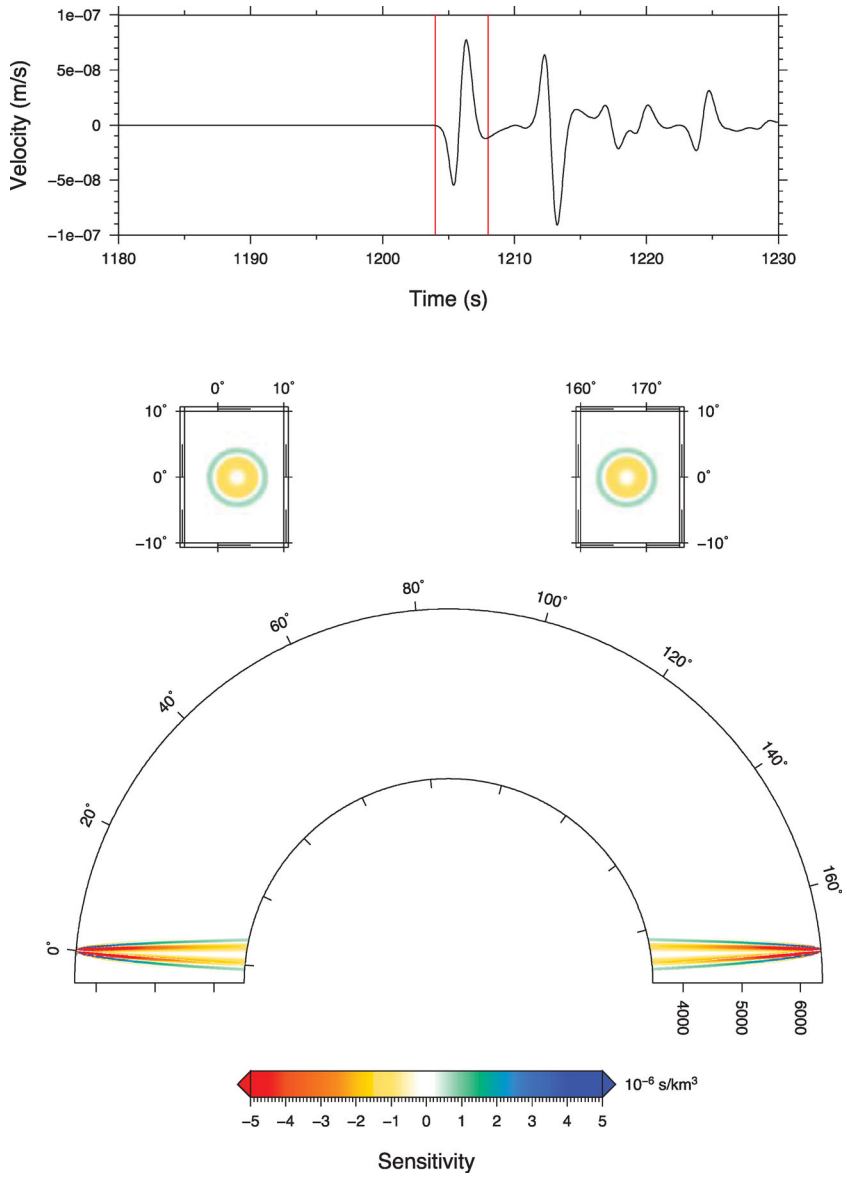


**Figure 7.** *PKP*df synthetic bandpass filtered between 0.1 and 1.0 Hz at 170° epicentral distance with an explosive source at 20 km depth (top panel). Cross-section in the great-circle plane (bottom panel) and map view at 2870 km depth (middle panel) of the traveltime sensitivity kernel for *P*-wave velocity for a *PKP*df phase (the selected window is shown with red lines on the synthetic).

the upper and lower zone when we interpolate. In this paper, for simplicity, we show the strains in the upper zone except the case for the surface.

The Green's functions are calculated for the ak135 reference Earth model (Kennett *et al.* 1995) with a step of 0.1° in distance, 20 km in depth from the surface down to the bottom of the mantle, and 0.05 s in time, for frequencies up to 1.25 Hz. These Green's functions are then stored on a disk.

## 4 INTERPOLATION OF GREEN'S FUNCTIONS

While the calculation of partial derivatives with the SGT database approach is very efficient, it is still limited by the number of SGT that must be stored and accessed during execution. Kernels are usually computed in a fine 3-D grid, and we require access to both SSGT and TSGT inside each element of this grid, which means that we must compute and store the SGT with a fine distance sampling. For example, in their computation of traveltime kernels, Zhao & Chevrot (2011b) used a SGT grid with a distance step as small as 0.01° for 8 s period kernels. Such a fine distance sampling requires both a significant volume of storage and reading large flows of input files during the computations. We will now present the results of a first attempt to reduce very significantly the size of the SGT database, while keeping the accuracy of the resulting kernels.

The interpolation of uniformly sampled and non-aliased data is straightforward, and can be performed by a SINC filter in the frequency domain (e.g. Shannon 1949; Unser 2000)

$$G(\omega, \theta) = \sum_j G(\omega, j\Delta\theta)\mathrm{sinc}\left(\frac{\theta}{\Delta\theta} - j\right), \tag{47}$$

where

$$\mathrm{sinc}(x) = \frac{\sin(\pi x)}{\pi x}. \tag{48}$$

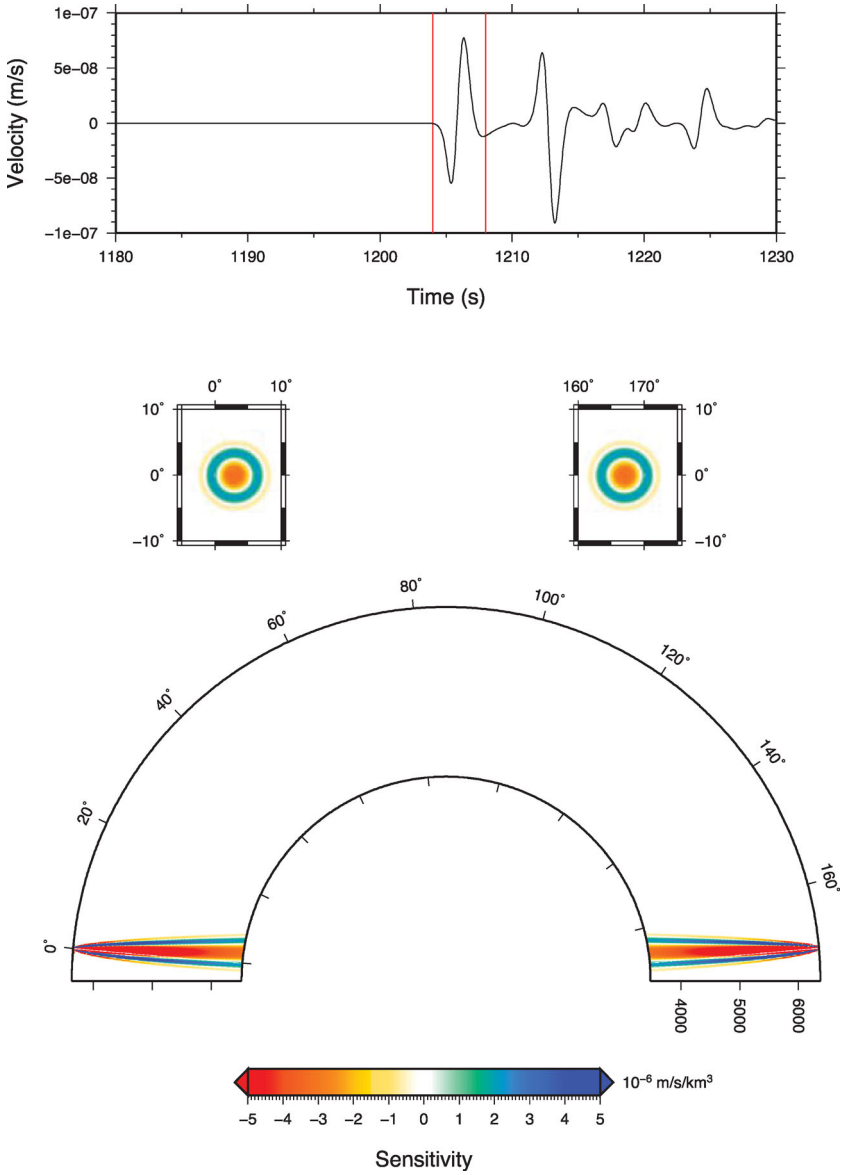


**Figure 8.** *PKP*df synthetic bandpass filtered between 0.1 and 1.0 Hz at 170° epicentral distance with an explosive source at 20 km depth (top panel). Cross-section in the great-circle plane (bottom panel) and map view at 2870 km depth (middle panel) of the amplitude sensitivity kernel for *P*-wave velocity for a *PKP*df phase (the selected window is shown with red lines on the synthetic).

A 20° distance range is typically considered to perform the interpolations. Since a spatial sampling of $\Delta\theta$ introduces a repetition of the spectrum with period $1/\Delta\theta$, spatial aliasing will occur if wavenumbers larger than $1/2\Delta\theta$ (Nyquist wavenumber) contribute to the signal. In other words, to avoid aliasing, the spatial sampling must satisfy

$$\Delta\theta \leq \frac{T_{\min}}{2p_{\max}} = \frac{\lambda_{\min}}{2}, \tag{49}$$

with $T_{\min}$ the shortest period and $p_{\max}$ the maximum slowness in the signal. For example, a 1 s *P* wave recorded at an epicentral distance of 65° has a slowness of 6.5 s deg$^{-1}$ and $\Delta\theta$ must be smaller than 0.08°. Obviously, this minimum sampling interval can be doubled if we consider waves with a dominant period of 2 s. Fig. 2(a) shows the results of interpolating 1 s SSGT around an epicentral distance of 65° with a distance sampling of 0.25°. The interpolated traces are distorted by spatial aliasing and cannot be used to compute partial derivatives. For a *PKP*df phase at 160° with a slowness of 1.1 s deg$^{-1}$, the spatial sampling must be smaller than 0.45°. Fig. 3(a) shows the results of interpolating 1 s SSGT around an epicentral distance of 170°. As expected, the interpolated traces are very accurate and it is thus possible to interpolate SGTs to compute *PKP* partial derivatives from a SGT database computed every 0.25°.

From these simple considerations, it can be seen that the computation of 3-D kernels for teleseismic *P* waves at frequencies up to 1 Hz and for any distance would require a database of SGTs sampled at about 0.05°. This would already constitute a significant improvement over our preliminary implementation which was based upon a distance sampling of 0.01°. However, it is possible to use a database with an even coarser sampling by reducing the spatial bandwidth before the interpolation. This is done by introducing a move-out correction with a slowness reduction based upon the theoretical ray parameter of the seismic phase. After correction, the seismic waves (for example the *P* waves) are aligned on all the records and their apparent slowness is then zero. The relation (49) is then satisfied for much larger spatial sampling. As can be seen in Fig. 2(b) the introduction of the normal move-out correction allows us to retrieve perfectly the *P* wave Green's functions at any intermediate location between the regularly sampled distances in the database. Using this trick, we are thus able to reduce the number of stored SGTs in the database by a factor of 25, which reduces very significantly the size of the database and the volume of input data to be read during the computation of the partial derivatives. The accuracy of the interpolation scheme is demonstrated by a test around the *PKP* triplication, where the seismic wavefield shows extreme complexities (Fig. 4). We are thus very confident that accurate partial derivatives can be obtained for any type of wave even when using a coarse grid for the SGT database.

It is interesting to note that the computation of kernels based upon the adjoint method (e.g. Nissen-Meyer *et al.* 2007a,b) also requires storing the direct and adjoint wavefields on a fine grid. It is likely that the interpolation of strain tensors would also significantly speed up the computations of partial derivatives using the adjoint method.

## 5 OPTIMIZATION OF THE ALGORITHM

The simplest algorithm to compute 3-D kernels is to define a large domain surrounding the source–receiver great circle plane inside which the values of the derivatives are systematically calculated. However, these values are actually significant only in a much smaller volume, which is defined by the first Fresnel zone. For most classical waves, such as the *P* or *S* waves, very small values are also found along the reference path given by ray theory, and the kernels typically have a banana–doughnut shape (Dahlen *et al.* 2000). This suggests that it is not necessary to compute the partial derivatives systematically inside a large domain, which led us to seek a more efficient and yet simple algorithm.

Our algorithm starts by computing, at each depth, the values of the kernel along the source–receiver great circle plane. We select along this line the points where the absolute value of the kernel exceeds 0.5 per cent of the maximum absolute value to define, at each depth, a mask that will be used for the adjacent planes. This mask is determined to closely follow the shape of the kernel. If the computed values are still above the threshold at one of the edges

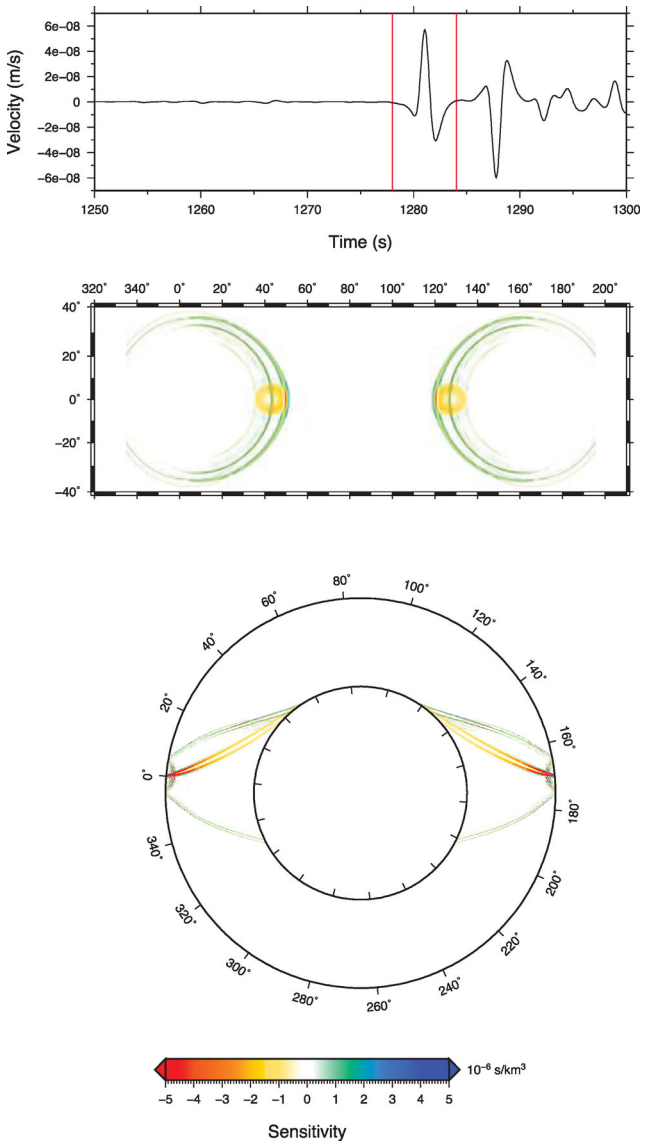


**Figure 9.** *PKP*ab synthetic bandpass filtered between 0.1 and 1.0 Hz at 170° epicentral distance with an explosive source at 20 km depth (top panel). Cross-section in the great-circle plane (bottom panel) and map view at 2870 km depth (middle panel) of the traveltime sensitivity kernel for *P*-wave velocity for a *PKP*ab phase (the selected window shown as red lines in the synthetic).

of the mask, the computation is extended along this direction. This allows the method to adapt to complicated kernel geometries such as the one for *PP* waves, for example. Fig. 5 shows the example of a kernel for a 10-s period *PP* wave at 200 km depth computed with this algorithm. As can be seen, this algorithm is able to capture and follow the complex shape of the kernel. This new implementation is interesting because it allows us to diminish the number of computed points by a factor of about 4, without losing any information.

## 6 EXAMPLES OF 3-D FRÉCHET KERNELS

We will now illustrate our approach by showing examples of traveltime, amplitude and waveform Fréchet kernels for different types of compressional waves. In these computations, we use an explosive source at 20 km depth, and only consider the dependence on $\alpha$, the *P*-wave velocity. A finite frequency traveltime anomaly $\delta T$ is

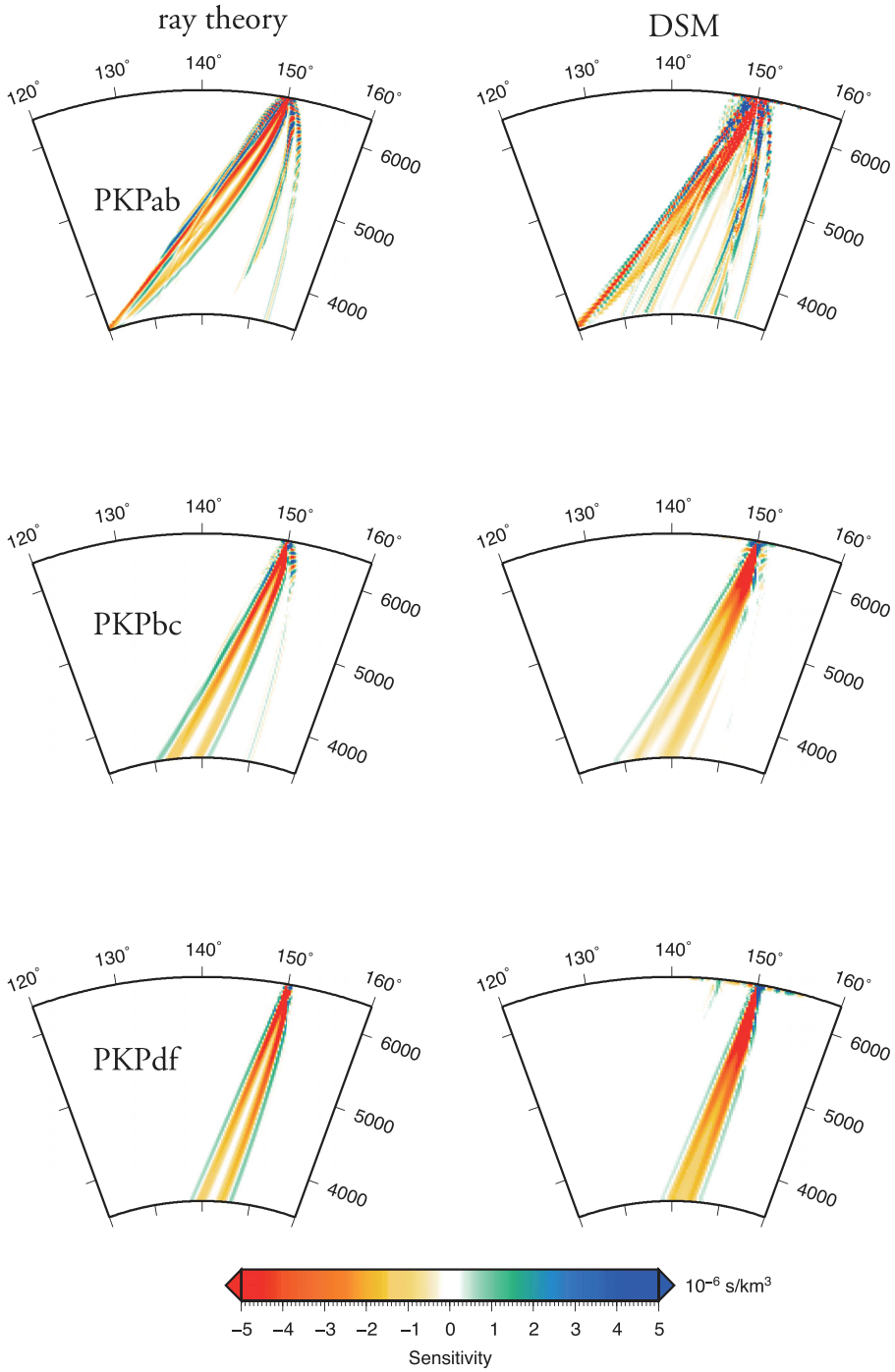


**Figure 10.** Cross-section comparison between traveltime kernels for *P*-wave velocity computed with ray theory (left-hand side) and with DSM (right-hand side) for *PKP*ab (top panel), *PKP*bc (middle panel) and *PKP*df (bottom panel) at 150° distance with an explosive source at 20 km depth.

measured by taking the maximum of the cross-correlation function between an observed and a reference seismic phase, inside the time window between $t_1$ and $t_2$. This time window is visually or automatically (Maggi *et al.* 2009) selected by picking the beginning and end of the seismic phase of interest on the synthetic trace. The sensitivity kernels are computed inside a spherical grid with a step of 0.25° in latitude and longitude and 40 km in radius for frequencies up to 1.25 Hz. In all our computations, we considered an explosive source at the north pole and at 20 km depth.

### 6.1 *PKP* kernels

*PKP* waves are compressional waves that travel through Earth's core. Depending on the epicentral distance, three different *PKP* branches can be recorded: the *PKP*ab, *PKP*bc, and *PKP*df branches (Fig. 6). Among these, *PKP*df is the only one that samples the inner core. The *PKP*ab phase mostly samples the shallow part of the outer core while the *PKP*bc phase samples the deeper part. The number of *PKP* phases that can be observed depends on both epicentral

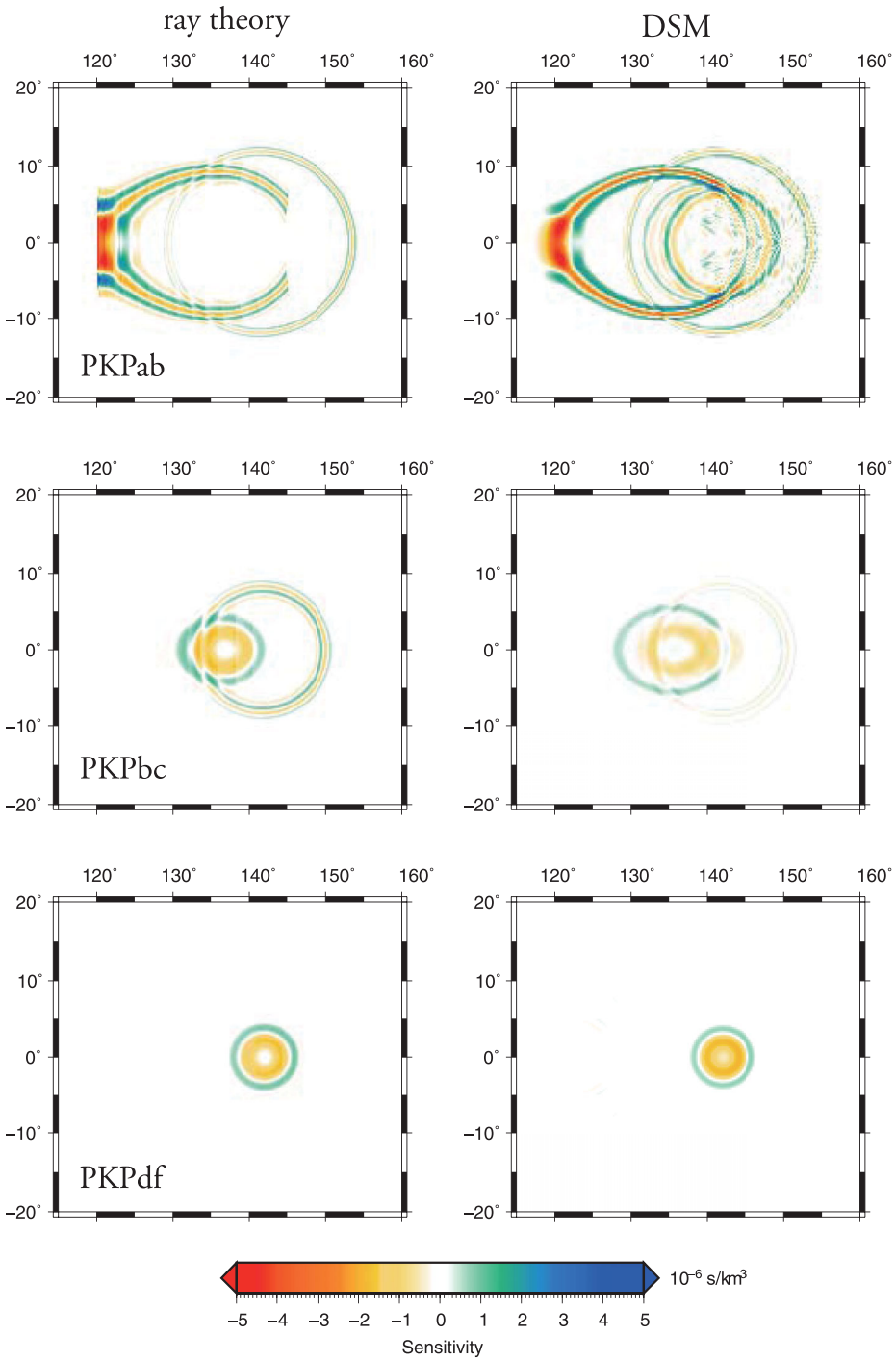


**Figure 11.** Comparison between traveltime kernels at 2870 km depth for *P*-wave velocity computed with ray theory (left-hand side) and with DSM (right-hand side) for *PKP*ab (top panel), *PKP*bc (middle panel) and *PKP*df (bottom panel) at 150° distance with an explosive source of 20 km depth.

distance and depth. At the free surface and for a shallow source, the three phases are simultaneously present only in the distance range 142–155°, often referred to as the *PKP* triplication. A global data set of *PKP* traveltimes that could be exploited in the framework of finite-frequency tomography has been recently obtained by Garcia *et al.* (2006).

Following the asymptotic approach introduced by Dahlen *et al.* (2000), Calvet & Chevrot (2005) showed that *PKP* traveltime kernels are complicated by interference effects between the different *PKP* branches. In addition, they found that the asymptotic approach suffers from serious limitations because it cannot describe the diffraction of the *PKP*ab phase at the CMB, and because the computation of *PKP* amplitudes close to the B-caustic breaks down with ray theory. Liu & Tromp (2008) determined *PKP* kernels from complete forward and adjoint wavefields computed using the spectral element method. They found that *PKP*ab, in contrast to *PKP*df, has sensitivity to structure outside the typical banana–doughnut kernel shape, a feature that they did not try to further elucidate. However, their computations were performed for 9 s dominant period *PKP* waves, well above the periods at which these phases are typically observed.

We show sensitivity kernels only in the mantle part in this paper since no significant heterogeneity is expected inside the outer core. We computed sensitivity kernels for traveltime and amplitude of a 1 s *PKP*df wave at a distance of 170° (Figs 7 and 8), using the precomputed SGT database obtained with DSM. Because the *PKP*df

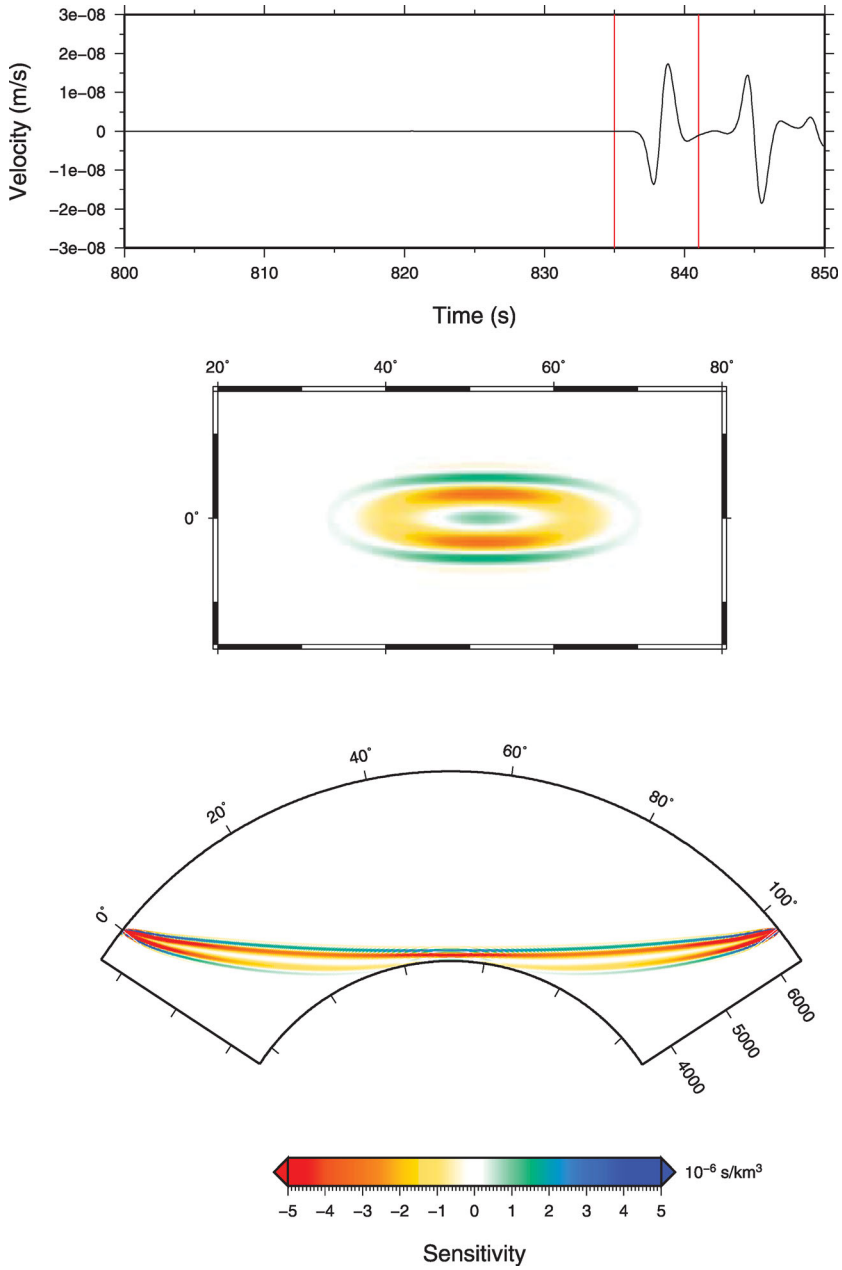


**Figure 12.** $P_{diff}$ synthetic bandpass filtered between 0.1 and 1.0 Hz at an epicentral distance of 103.3° with an explosive source at 20 km depth (top panel). Cross-section in the great-circle plane (bottom panel) and map view at 2880 km depth (middle panel) of the traveltime sensitivity kernel for *P*-wave velocity for a $P_{diff}$ wave The selected window is shown with red lines on the synthetic.

phase travels faster than the *PKP*ab phase, scattered *PKP*ab waves arrive much later than the *PKP*df wave and there is no coupling between the two branches. Consequently, *PKP*df kernels display simple and classical shapes, very similar to those of the *P* wave. In comparison, the traveltime kernel for *PKP*ab at 170° (Fig. 9) appear much more complicated. The strong semi-circular streaks are produced by the contribution of scattered *PKP*bc and *PKP*df phases (and their depth phases), which have very strong amplitudes close to the B-caustic, as can be seen in Fig. 6. However, since their contributions to the *PKP*ab kernels oscillate rapidly, these scattered phases are only sensitive to the very short wavelengths of the power spectrum of the spatial heterogeneity. Another notable feature is that the Fresnel zones of the different *PKP* waves differ in size and shape, even though the different waves have a similar frequency content. A comparison of traveltime kernels for the three *PKP* branches at 150° obtained using ray theory (Calvet & Chevrot 2005) and using DSM (this study) is shown in Figs 10 and 11. It is interesting to note that while the *PKP*df kernels are very similar, the *PKP*ab and *PKP*bc kernels show significant differences. These differences are direct consequences of the different approximations involved in ray theory. First, the diffraction of *PKP*ab on the CMB is not accounted for by ray theory and a sharp cut-off is observed at the edges of the shadow zone of *PKP*ab. Second, the amplitudes of *PKP*ab and *PKP*bc close to the B-caustic determined by ray theory from the geometrical spreading of these phases are incorrect. This introduces strong biases in the traveltime kernels of *PKP*ab and *PKP*bc.

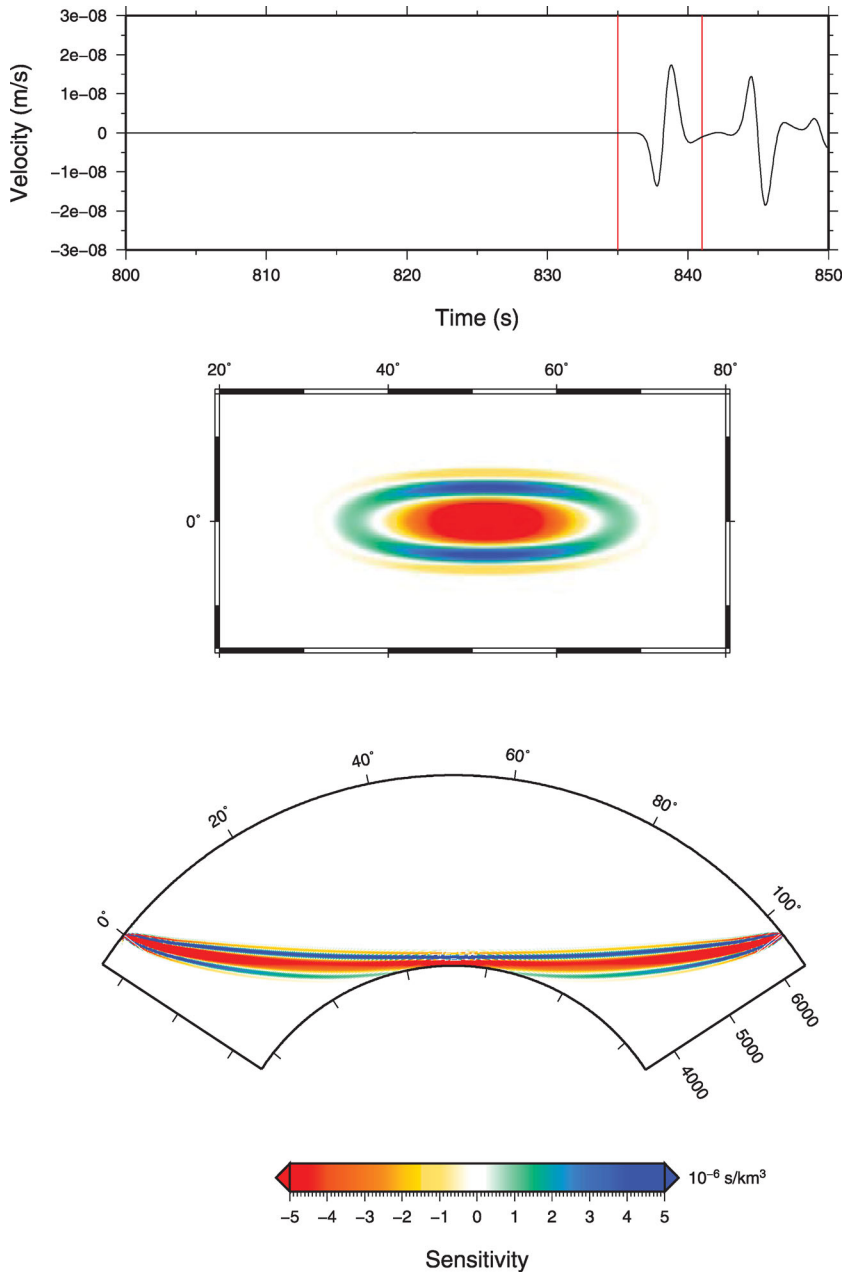


**Figure 13.** $P_{diff}$ synthetic bandpass filtered between 0.1 and 1.0 Hz at an epicentral distance of 103.3° with an explosive source at 20 km depth (top panel). Cross-section in the great-circle plane (bottom panel) and map view at 2880 km depth (middle panel) of the amplitude sensitivity kernel for *P*-wave velocity for a $P_{diff}$ wave The selected window is shown with red lines on the synthetic.

Finally, it can be seen that scattered depth phases contribute to the *PKP*ab kernel. These depth phases are not taken into account in the ray theory computations. This clearly emphasizes another limitation of the asymptotic approach to compute sensitivity kernels, as this requires modelling all the seismic phases that can potentially interfere and contribute to the finite-frequency traveltime measurement in the time window of interest. When the wavefield is complicated, this can be cumbersome and there is always the risk of omitting a phase that makes a significant contribution. Obviously, full waveform modelling approaches such as DSM do not suffer from this limitation.

Since they are mostly sensitive to lowermost mantle structure, *PKP*ab-*PKP*df and *PKP*bc-*PKP*df differential traveltimes have been used to constrain the heterogeneities in the D″ layer (e.g. Garcia *et al.* 2009). Kernels for these differential traveltimes are simply obtained by computing the difference of the kernels corresponding to the two *PKP* branches involved (Calvet & Chevrot 2005).

### 6.2 $P_{diff}$ kernels

*P* waves diffracted along the core–mantle boundary (CMB) are also very sensitive to heterogeneity at the base of the mantle. However, because these waves cannot be described by ray theory, they have been rarely used in tomographic studies. For example, Karason & van der Hilst (2001) used three $P_{diff}$ kernels computed by normal mode coupling (Zhao *et al.* 2000) which were interpolated to determine $P_{diff}$ kernels at specific distances. This basic approach was the first step to account for the finite Fresnel volumes of diffracted waves, even though the frequency content of the analysed $P_{diff}$ records and those used in the computed kernels did not match. Figs 12 and 13 show respectively the traveltime and amplitude kernels of a 1 s $P_{diff}$ at 103° distance. These kernels clearly demonstrate that these waves have a strong sensitivity to heterogeneity in the lowermost mantle, and that the depth of the maximum sensitivity strongly varies as a function of the dominant period of the

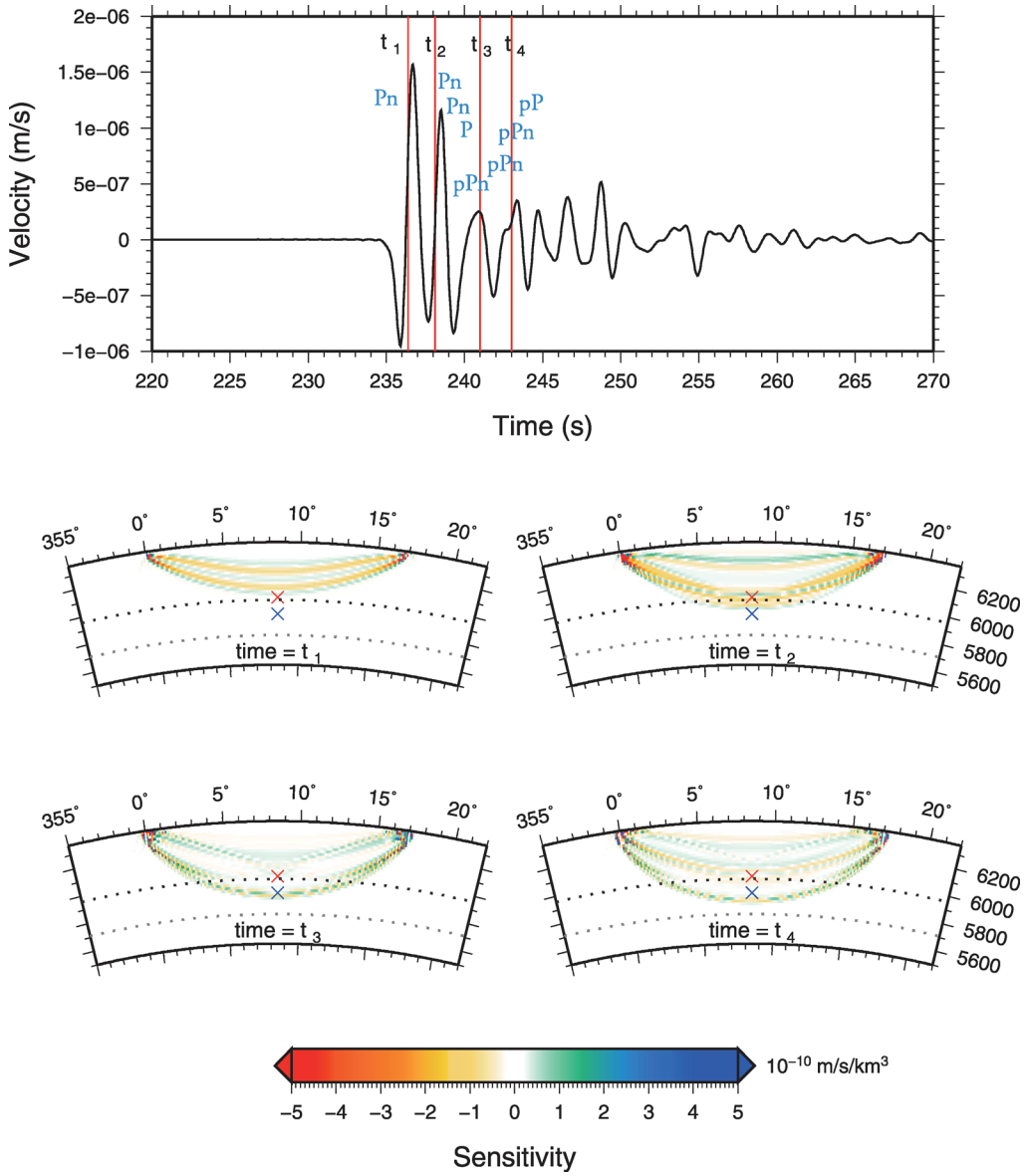


**Figure 14.** Waveform partial derivatives bandpass filtered between 0.1 and 1.0 Hz for *P*-wave velocity for a receiver located 17° from an explosive source at 20 km depth at time $t_1 = 236.2$ s, $t_2 = 238.1$ s, $t_3 = 241.0$ s and $t_4 = 243.0$ s. The top trace shows the vertical component of a synthetic seismogram at a receiver located 17° from the source.

diffracted wave. Indeed, in their computations based upon normal mode summation down to 8 s, Zhao & Chevrot (2011b) observed that the maximum sensitivity of $P_{diff}$ waves was about 500 km thick just above the CMB, while in our computations made around 1 s period, we found that the maximum sensitivity is thinner to the CMB (about 100–200 km thick above the CMB). Owing to the variable thickness of the D″ layer and to the strong, small-scale, variability of heterogeneities at the base of the mantle (Garcia *et al.* 2009), the traveltime and amplitude anomalies of $P_{diff}$ phases are expected to vary strongly with their frequency content. It is thus crucial to build a high-quality database of finite-frequency measurements of traveltime and amplitude anomalies of diffracted waves and to account for these finite-frequency effects in inversions if we are to improve the resolution of tomographic models at the base of the mantle.

## 7 WAVEFORM PARTIAL DERIVATIVES

Besides velocity tomography, another approach to image mantle structures is to exploit waves scattered by mantle discontinuities or localized heterogeneities by migration or waveform inversion. In this case, relation (1 or 16) can be used directly to relate the scattered wavefield to the velocity perturbations in the underlying medium. Very often, this is implemented by using simplified migration schemes, relying on asymptotic approximations of the seismic wavefield or by trial and error fitting of 1-D synthetic seismograms. In the following, we examine two different source–receiver configurations that have been used to constrain transition zone discontinuities and D″ layer structure by waveform inversion. Note that for the past several years, three of the authors of the present paper have used these partial derivatives to conduct waveform inversion for the localized 1-D *S*-wave velocity structure of D″ (Kawai *et al.* 2007a,b, 2009, 2010; Konishi *et al.* 2009; Kawai & Geller 2010a,b,c) and for the localized 1-D elastic and anelastic structure of the MTZ (Fuji *et al.* 2010). Note that Kawai & Geller (2010b) inverted waveform data to directly infer anisotropic structure.

### 7.1 *P* waves around the 410-discontinuity triplication

Detailed velocity profiles have been obtained from the exploitation of *P* wave records in different tectonic regions (e.g. Burdick

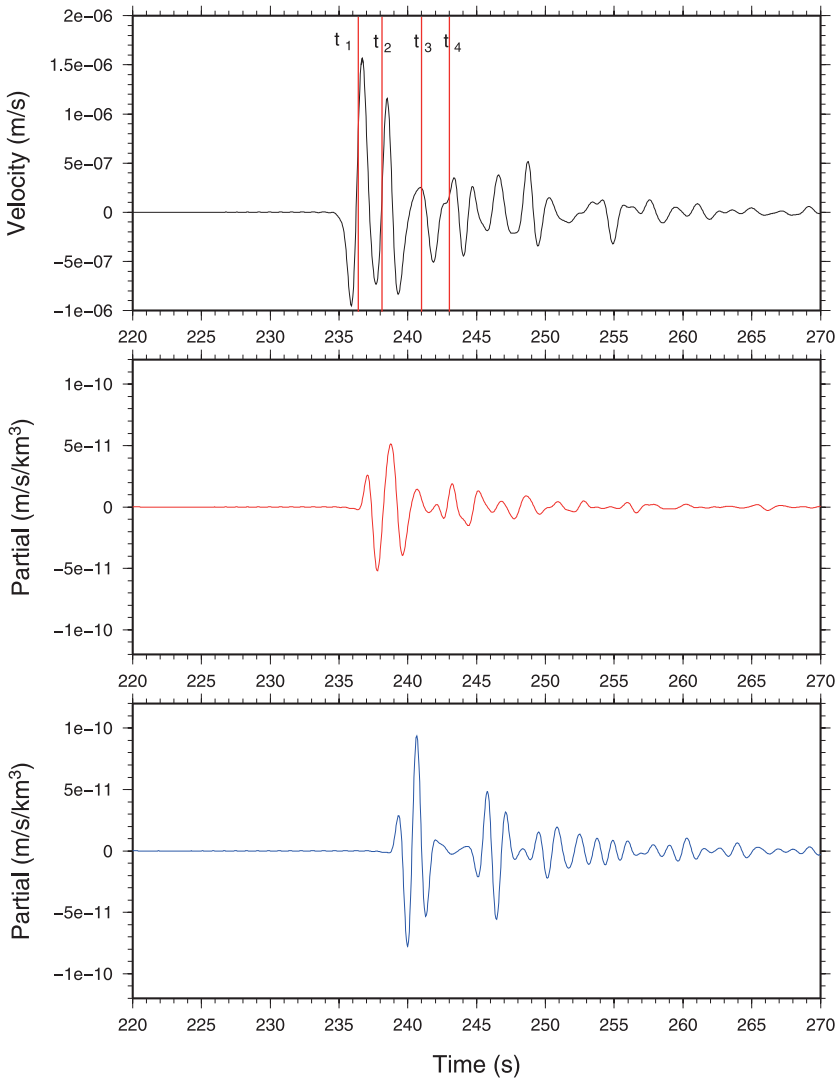


**Figure 15.** Waveform partial derivatives for *P*-wave velocity at a point located at 8.5° from the source at 20 km depth at 400 km depth (red) and at 500 km depth (blue). The signals were bandpass filtered between 0.1 and 1.0 Hz. The position of these points are marked with the red and blue crosses in Fig. 14. The top trace shows the synthetic seismogram at a receiver located 17° from the source.

& Helmberger 1978; Given & Helmberger 1980; Walck 1984), by comparing observed *P* waveforms to synthetic seismograms computed with a 1-D modelling approach. These models yielded important constraints on the thickness of the high-velocity lid, on the intermittent existence of a low-velocity zone around 150 km depth, and on the depth of transition zone discontinuities, all of which are important clues for understanding mantle dynamics.

We computed the Fréchet kernel given by eq. (16) for the vertical component waveform recorded at a distance of 17° from the source. Fig. 14 shows the values of the partial derivative with respect to $\alpha$ in the source–receiver plane at different times. The snapshots correspond to times $t_1 = 236.2$ s, $t_2 = 238.1$ s, $t_3 = 241.0$ s and $t_4 = 243.0$ s. The top trace shows the vertical component of the synthetic seismogram around the first *P*-wave arrival. At this epicentral distance, the *P* waveform is very complicated. It is a superposition of arrivals that interfere in the time domain. This complexity is produced by the 410 discontinuity, which is responsible for a triplication of the *P* wave. The first arrival is a *P* wave that propagates purely in the upper mantle, which is followed by a wave that has been reflected at the top of the 410 discontinuity and by a wave refracted at the discontinuity, that propagates below the 410 discontinuity. These different seismic arrivals can be clearly identified in the waveform Fréchet kernels at onset times $t_1$, $t_2$ and $t_4$. It is interesting to note that the significant values of the waveform partial derivative at this particular distance span a large depth interval, from the surface down to about 600 km depth. This confirms that waveforms recorded around this epicentral distance range are particularly well adapted to constrain upper mantle velocity profiles. The partial derivatives at mid-distance between the source and the receiver at 400 (red cross in Fig. 14) and 500 km depth (blue cross in Fig. 14) are shown in Fig. 15. While sensitivity can be strong at both locations at some particular onsets, the two Fréchet derivatives have very different temporal variations. This demonstrates that a perturbation of seismic velocity inside the mantle has a signature on the seismograms that strongly depends on its location. Waveform inversion identifies these signatures inside observed seismological records to obtain the distribution of velocity perturbations inside Earth's mantle. In contrast to traveltime kernels, for which sensitivity is broadly distributed over the first Fresnel zones, waveform kernels thus have a much better resolution potential but it is essential

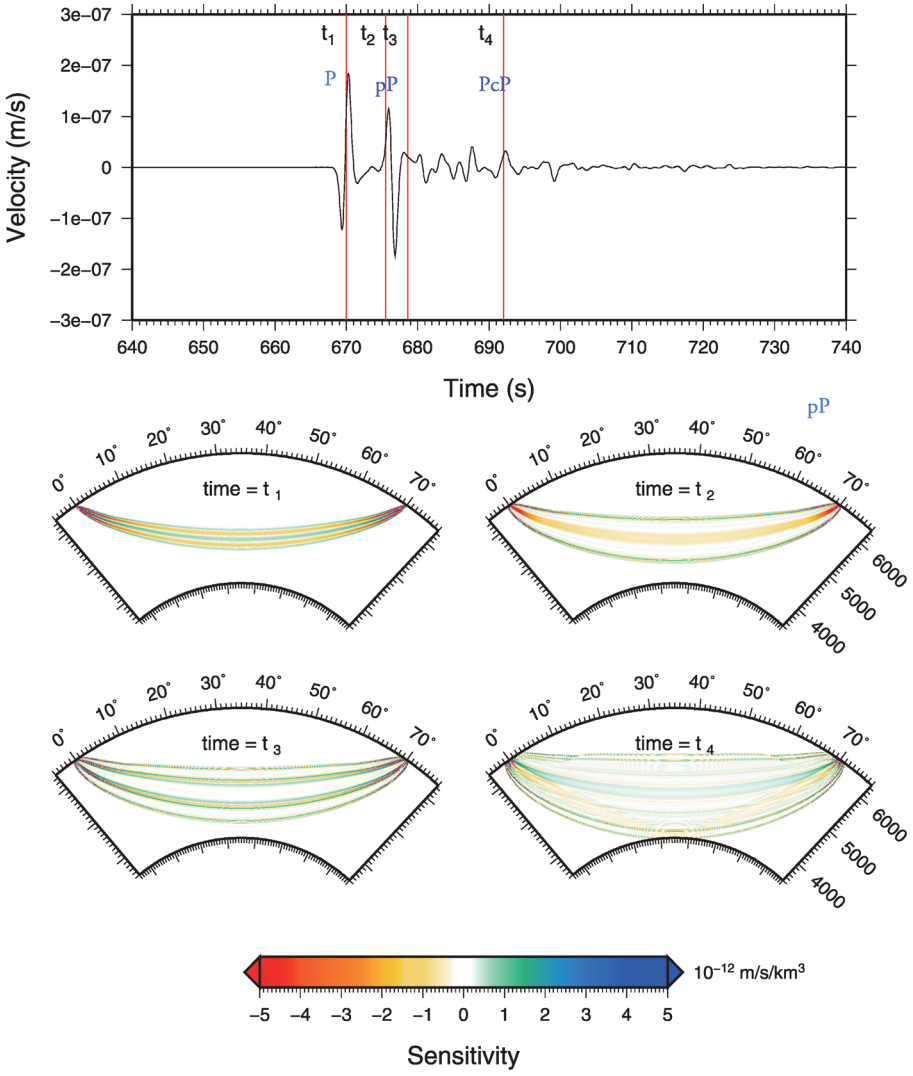


**Figure 16.** Waveform partial derivatives bandpass filtered between 0.1 and 1.0 Hz for *P*-wave velocity for a receiver located 70° from the source whose depth is 20 km at time $t_1 = 670.0$ s, $t_2 = 675.5$ s, $t_3 = 678.6$ s and $t_4 = 692.0$ s. The top trace shows the vertical component of a synthetic seismogram at a receiver located 70° from the source.

to consider long time windows to optimize this spatial resolution. In our example, the partial derivatives are computed with respect to a spherically symmetric reference medium. These waveform kernels can be used to migrate seismic waveforms to obtain high resolution images of small-scale mantle heterogeneities and/or seismic discontinuities. Full iterative waveform inversion would require computing SGTs in 3-D models, which is clearly beyond the scope of this study.

### 7.2 *PcP* precursors

The base of the mantle is another part of the Earth's interior that has also been extensively studied by waveform inversion. For example, for epicentral distances between 50 and 90°, in the time interval between *P* and *PcP* waves, it is possible to detect *PcP* precursors corresponding to waves reflected on top of an ultra low velocity layer (e.g. Persh *et al.* 2001) or scattered by strong

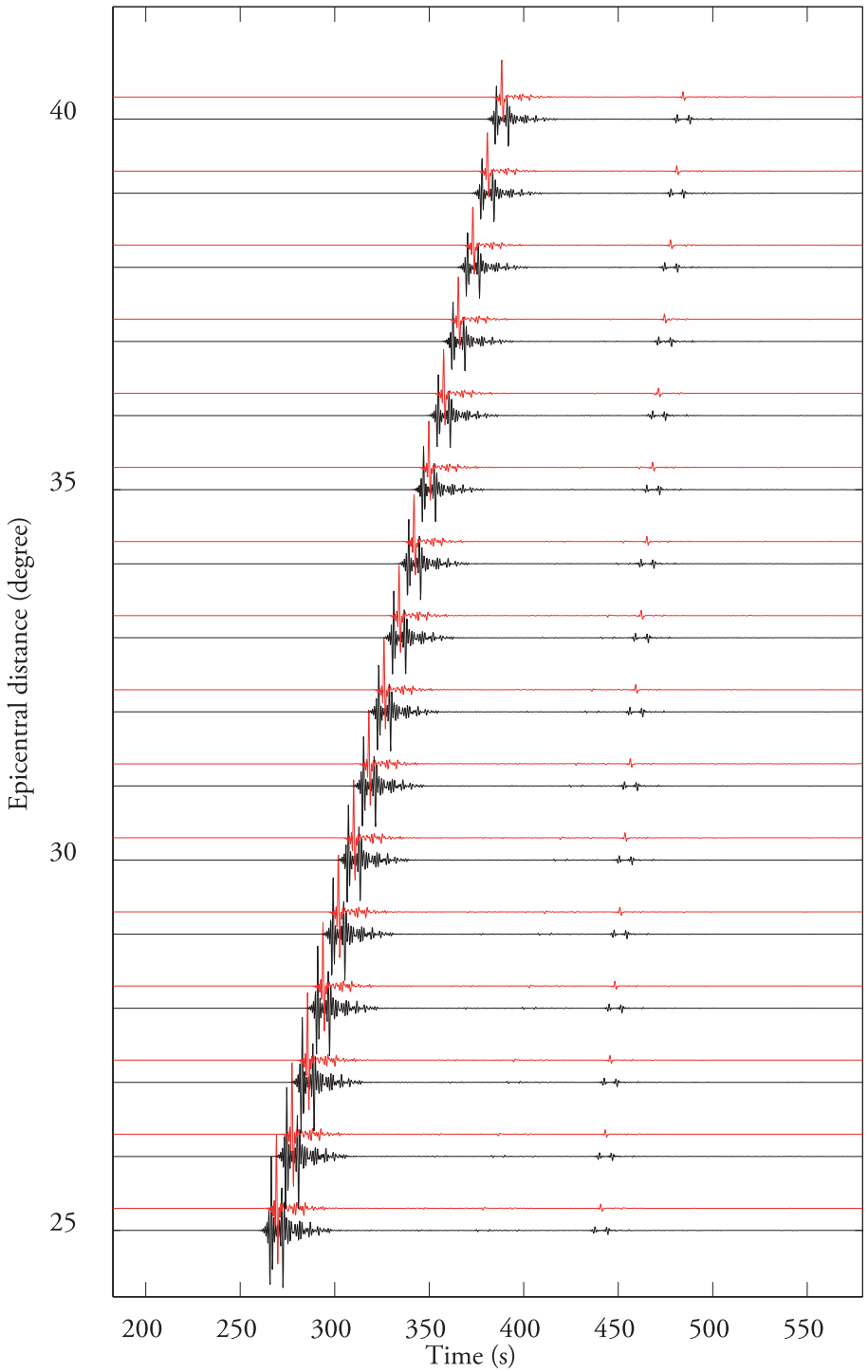


**Figure 17.** Single-Side Green's Tensors (red lines) and Two-Side Green's Tensors (black lines) at 940 km depth calculated up to 1.25 Hz and filtered between 0.1 and 1.0 Hz for an explosive source at 35° distance. The direct *P* wave arrives around $t = 340$ s.

heterogeneities in the D′′ layer (e.g. Freybourger *et al.* 2000; Kito & Krüger 2001).

Fig. 16 shows snapshots corresponding to times $t_1 = 670.0$ s, $t_2 = 678.6$ s, $t_3 = 684.2$ s and $t_4 = 691.7$ s, for the partial derivative $K^u_\alpha$, computed for a receiver located 70° from the source. The top trace shows the vertical component of the synthetic seismogram around the *PcP* arrival. The partial derivatives at $t = t_1$ and $t = t_2$ clearly show that the sensitivity is concentrated inside the first Fresnel zone of the *P* wave. The partial derivative at $t = t_4$ shows some sensitivity inside the Fresnel zone of the *PcP* wave, but significant sensitivity is also observed at the top of the lower mantle. This suggests that scattering at the top of the lower mantle could also produce a signal in the *PcP* precursor time window. This can be seen in Fig. 17 where we have plotted the SSGT and TSGT at 940 km depth at mid distance between the source and the receiver. The *P* waves on each component arrive around 340 s, which means that *P* waves scattered in this part of the mantle will indeed arrive between the *P* and *PcP* waves. The values of the partial derivatives in the mid-mantle are actually larger than those in the bottom part of the lower mantle. Scattered waves resulting from *P*–*P* scattering on heterogeneities in the mid-mantle travel through a caustic, and their waveforms are thus expected to be the Hilbert transform of either the direct *P* wave or the *PcP* wave. Interestingly, such a difference in waveform has been observed by Freybourger *et al.* (2000), which could suggest that the *PcP* precursors that they detected for paths going from Kuril Islands earthquakes to stations in western Europe are actually located in the mid-mantle and not at the base of the mantle.

## 8 CONCLUSIONS

We have developed an efficient method to compute accurate 3-D partial derivatives for delay-time, amplitude and waveform anomalies with respect to *P*-velocities up to 1 s period. This method relies on the exploitation of a precomputed database of SGTs that are calculated with the DSM. To be able to compute kernels for high-frequency teleseismic *P* waves, we introduced several improvements to the original implementation by Zhao & Chevrot (2011a,b). First, we derived the specific forms of the Green's tensors that are involved in the computation of *P* wave kernels. This allowed us to reduce drastically the number of SGT components that need to be computed and stored: from 10 to 1 for SSGT, and from 20 to 4 for TSGT. Second, to limit the size of the SGT database, we showed that it is possible to obtain accurate results by interpolating SGTs computed in a coarse grid. Compared to our initial implementation, we were able to reduce the size of the SGT database by a factor 25 without loss of accuracy. This considerably speeds up the computations. Finally, we have optimized the algorithm to compute the values of partial derivatives only where they are significant. This reduces the number of computations by a factor 4. The combination of these different optimizations now allows us to compute partial derivatives for high-frequency teleseismic body waves with very modest computer resources. It takes around 64 days on a single processor to compute *P*-wave SGTs (1 SSGT and 4 TSGTs) with a length of 1638.2 s up to 1.25 Hz for a grid sampling of 20 km along the vertical dimension and 0.2° along distance. Storing those SGTs requires around 5 Gb of disk space. These numbers are considerably reduced when performing computations at lower frequencies. For example, the same computation would take only 16 days for a frequency cut-off of 0.625 Hz. Once the SGTs are obtained, the computation of a 1 Hz *PKP* kernel takes around 30 min on a single processor. Using a moderate size cluster, our approach makes finite-frequency tomography feasible, even on rather large data sets.

We have computed traveltime and amplitude kernels for *PKP* phases up to 1 s period. We found that *PKP*ab and *PKP*bc kernels show significant differences compared to those computed with the asymptotic forms of the Green's tensors by Calvet & Chevrot (2005). This clearly demonstrates the limitations of the asymptotic approach introduced by Dahlen *et al.* (2000) to compute sensitivity kernels, even in the high frequency limit where ray theory is expected to give satisfactory solutions to the wave equation. Our approach also allows an efficient computation of waveform partial derivatives. Such quantities will be most useful for waveform inversion of high-frequency teleseismic *P* wave fields. For example, scattering points located at 400 and 500 km depth have very different temporal contributions to the waveform signal recorded at 17°. This clearly demonstrates that waveform inversion has the potential to resolve heterogeneities with a fine resolution, even with a limited number of records. In comparison, the sensitivity is more broadly distributed in traveltime kernels, and a fine spatial resolution can only be obtained with a very good path coverage. The waveform partial derivatives computed in the spatial and temporal window corresponding to *PcP* precursors show a complex distribution of sensitivity. In particular, sensitivity is particularly strong in the mid-mantle, way above the base of the mantle where all studies placed the origin of these *PcP* precursors. In studies of deep Earth structures, it is thus important to consider accurate and complete partial derivatives, which are often complex, and sometimes counter-intuitive. Simple interpretations of seismological records based upon 1-D modelling and/or asymptotic theory can sometimes be seriously misleading.

## ACKNOWLEDGMENTS

The authors thank Marie Calvet for discussions about the *PKP* kernels, Tarje Nissen-Meyer for discussions about the kernel calculation in general, and Vadim Monteiller for fruitful discussions about SGT calculation. KK is supported by a JSPS Fellowship for Young Scientists. This study was funded by the ANR-blanc project PYROPE (ANR-09-BLAN-0229) and also was supported by a grant from the JSPS (No.22540433). LZ is supported by a Career Development Award of Academia Sinica in Taiwan.

## REFERENCES

Bijwaard, H., Spakman, W. & Engdahl, E.R., 1998. Closing the gap between regional and global travel time tomography, *J. geophys. Res.,* **103,** 30 055–30 078.

Burdick, L.J. & Helmberger, D.V., 1978. Upper mantle P velocity structure of western United States, *J. geophys. Res.,* **83,** 1699–1712.

Calvet, M. & Chevrot, S., 2005. Traveltime sensitivity kernels for PKP phases in the mantle, *Phys. Earth planet. Inter.,* **153,** 21–31.

Chen, P., Jordan, T.H. & Zhao, L., 2007. Full three-dimensional tomography: a comparison between the scattering-integral and adjoint-wavefield methods, *Geophys. J. Int.,* **170,** 175–181.

Dahlen, F.A., Hung, S.-H. & Nolet, G., 2000. Fréchet kernels for finite-frequency traveltimes – I. Theory, *Geophys. J. Int.,* **141,** 157–174.

Favier, N., Chevrot, S. & Komatitsch, D., 2004. Near-field influence on shear wave splitting and travel-time sensitivity kernels, *Geophys. J. Int.,* **153,** 213–228.

Fichtner, A., Kennett, B.L.N., Igel, H. & Bunge, H.P., 2008. Theoretical background for continental and global scale full-waveform inversion in the time-frequency domain, *Geophys. J. Int.,* **175,** 665–685.

Freybourger, M., Chevrot, S., Kruger, F. & Achauer, U., 2000. A waveform migration for the investigation of P wave structure at the top of D′′ beneath northern Siberia, *J. geophys. Res.,* **106,** 4129–4140.

Fuji, N., Kawai, K. & Geller, R.J., 2010. A methodology for inversion of broadband seismic waveforms for elastic and anelastic structure and its application to the mantle transition zone beneath the Northwestern Pacific, *Phys. Earth planet. Inter.,* **180,** 118–137.

Garcia, R., Tkalcic, H. & Chevrot, S., 2006. A new global PKP dataset to study Earth's core and deep mantle, *Phys. Earth planet. Inter.,* **159,** 15–31.

Garcia, R., Chevrot, S. & Calvet, M., 2009. Statistical study of seismic heterogeneities at the base of the mantle from PKP differential traveltimes, *Geophys. J. Int.,* **179,** 1607–1616.

Geller, R.J. & Hara, T., 1993. Two efficient algorithms for iterative linearized inversion of seismic waveform data, *Geophys. J. Int.,* **115,** 699–710.

Geller, R.J. & Ohminato, T., 1994. Computation of synthetic seismograms and their partial derivatives for heterogeneous media with arbitrary natural boundary-conditions using the Direct Solution Method, *Geophys. J. Int.,* **116,** 421–446.

Geller, R.J. & Takeuchi, N., 1995. A new method for computing highly accurate DSM synthetic seismograms, *Geophys. J. Int.,* **123,** 449–470.

Given, J.W. & Helmberger, D.V., 1980. Upper mantle structure of northwestern Eurasia, *J. geophys. Res.,* **85,** 7183–7194.

Karason, H. & van der Hilst, R.D., 2001. Tomographic imaging of the lowermost mantle with differential times of refracted and diffracted core phases (PKP, Pdiff), *J. geophys. Res.,* **106,** 6569–6588.

Kawai, K. & Geller, R.J., 2010a. Waveform inversion for localized seismic structure and an application to D′′ structure beneath the Pacific, *J. geophys. Res.,* **115,** B031305, doi:10.1029/2009JB006503.

Kawai, K. & Geller, R.J., 2010b. The vertical flow in the lowermost mantle beneath the Pacific from inversion of seismic waveforms for anisotropic structure, *Earth planet. Sci. Lett.,* **297,** 190–198.

Kawai, K. & Geller, R.J., 2010c. Inversion of seismic waveforms for shear wave velocity structure in the lowermost mantle beneath the Hawaiian hotspot, *Phys. Earth planet. Inter.,* **183,** 136–142.

Kawai, K., Takeuchi, N. & Geller, R.J., 2006. Complete synthetic seismograms up to 2 Hz for transversely isotropic spherically symmetric media, *Geophys. J. Int.,* **164,** 411–424.

Kawai, K., Takeuchi, N., Geller, R.J. & Fuji, N., 2007a. Possible evidence for a double crossing phase transition in D′′ beneath Central America from inversion of seismic waveforms, *Geophys. Res. Lett.,* **34,** L09314, doi:10.1029/2007GL029642.

Kawai, K., Geller, R.J. & Fuji, N., 2007b. D′′ beneath the Arctic from inversion of shear waveforms, *Geophys. Res. Lett.,* **34,** L21305, doi:10.1029/2007GL031517.

Kawai, K., Sekine, S., Fuji, N. & Geller, R.J., 2009. Waveform inversion for D′′ structure beneath northern Asia using Hi-net tiltmeter data, *Geophys. Res. Lett.,* **36,** L20314, doi:10.1029/2009GL039651.

Kawai, K., Geller, R.J. & Fuji, N., 2010. Waveform inversion for S-wave structure in the lowermost mantle beneath the Arctic: implications for mineralogy and chemical composition, *Geophys. Res. Lett.,* **37,** L16301, doi:10.1029/2010GL043654.

Kennett, B.L.N., Engdahl, E.R. & Buland, R., 1995. Constraints on seismic velocities in the Earth from traveltimes, *Geophys. J. Int.,* **122,** 108–124.

Kito, T. & Krüger, F., 2001. Heterogeneities in D′′ beneath the southwestern Pacific inferred from scattered and reflected P-waves, *Geophys. Res. Lett.,* **28,** 2545–2548.

Konishi, K., Kawai, K., Geller, R.J. & Fuji, N., 2009. MORB in the lowermost mantle beneath the western Pacific: evidence from waveform inversion, *Earth planet. Sci. Lett.,* **278,** 219–225.

Liu, Q. & Tromp, J., 2008. Finite-frequency sensitivity kernels for global seismic wave propagation based upon adjoint methods, *Geophys. J. Int.,* **174,** 265–286.

Maggi, A., Tape, C., Chen, M., Chao, D. & Tromp, J., 2009. An automated time-window algorithm for seismic tomography, *Geophys. J. Int.,* **178,** 257–281.

Montelli, R., Nolet, G., Dahlen, F.A., Masters, G., Engdahl, E.R. & Hung, S.-H., 2004. Finite-frequency tomography reveals a variety of plumes in the mantle, *Science,* **303,** 338–343.

Nissen-Meyer, T., Fournier, A. & Dahlen, F.A., 2007. A 2-D spectral-element method for computing spherical-earth seismograms—I. Moment-tensor source, *Geophys. J. Int.,* **168,** 1067–1093.

Nissen-Meyer, T., Dahlen, F.A. & Fournier, A., 2007. Spherical-earth Frchet sensitivity kernels, *Geophys. J. Int.,* **168,** 1051–1066.

Persh, S.E., Vidale, J.E. & Earle, P.S., 2001. Absence of short-period ULVZ precursors to PcP and ScP from two regions of the CMB, *Geophys. Res. Lett.,* **28,** 387–390.

Shannon, C.E., 1949. Communication in the presence of noise, *Proc. IEEE,* **86,** 447–457.

Sieminski, A., Liu, Q., Trampert, J. & Tromp, J., 2007. Finite-frequency sensitivity of body waves to anisotropy based upon adjoint methods, *Geophys. J. Int.,* **171,** 368–389.

Suetsugu, D. *et al.*, 2005. Mantle discontinuity depths beneath the West Philippine Basin from receiver function analysis of deep-sea borehole and seafloor broadband waveforms, *Bull. seism. Soc. Am.,* **95,** 1947–1956.

Takeuchi, H. & Saito, M., 1972. Seismic surface waves, in *Methods in Computational Physics,* Vol. 11, pp. 217–295, ed. Bolt, B.A., Academic Press, New York, NY.

Takeuchi, N., Geller, R.J. & Cummins, P.R., 1996. Highly accurate P-SV complete synthetic seismograms using modified DSM operators, *Geophys. Res. Lett.,* **23,** 1175–1178.

Tromp, J., Tape, C.H. & Liu, Q., 2005. Seismic tomography, adjoint methods, time reversal, and banana-doughnut kernels, *Geophys. J. Int.,* **160,** 195–216.

Unser, M., 2000. Sampling – 50 years after Shannon, *Proc. IEEE,* **88,** 569–587.

van der Hilst, R.D., Widiyantoro, S. & Engdahl, E.R., 1997. Evidence for deep mantle circulation from global tomography, *Nature,* **386,** 578–584.

Walck, M.C., 1984. The P-wave upper mantle structure beneath an active spreading center—The Gulf of California, *Geophys. J. R. astr. Soc.,* **76,** 697–723.

Zhao, L. & Chevrot, S., 2011a. An efficient and flexible approach to the calculation of three-dimensional full-wave Fréchet kernels for seismic tomography — I. Theory, *Geophys. J. Int.,* **185,** 922–938.

Zhao, L. & Chevrot, S., 2011b. An efficient and flexible approach to the calculation of three-dimensional full-wave Fréchet kernels for seismic tomography — II. Numerical Results, *Geophys. J. Int.,* **185,** 939–954.

Zhao, L., Jordan, T.H. & Chapman, C.H., 2000. Three-dimensional Fréchet differential kernels for seismic delay times, *Geophys. J. Int.,* **141,** 558–576.

Zhao, L., Jordan, T.H., Olsen, K.B. & Chen, P., 2005. Frchet kernels for imaging regional Earth structure based on three-dimensional reference models, *Bull. seism. Soc. Am.,* **95,** 2066–2080.

Zhao, L., Chen, P. & Jordan, T.H., 2006. Strain Green tensors, reciprocity, and their applications to seismic source and structure studies, *Bull. seism. Soc. Am.,* **96,** 1753–1763, doi:10.1785/0120050253.